Quaternary Science Reviews 170 (2017) 250–268

Contents lists available at ScienceDirect

Quaternary Science Reviews

journal homepage: www.elsevier.com/locate/quascirev

Dynamics and sources of last glacial aeolian deposition in southwest France derived from dune patterns, grain-size gradients and geochemistry, and reconstruction of efficient wind directions

Luca Sitzia [a, *], Pascal Bertran [b, c], Adriana Sima [d], Philippe Chery [e], Alain Queffelec [c], Denis-Didier Rousseau [f, g]

[a] Universidad de Tarapacá, Instituto de Alta Investigación, Laboratorio de Análisis e Investigaciones Arqueométricas, Antofagasta 1520, 1010069 Arica, Chile
[b] INRAP, 140 Avenue Leclerc, 33130 Bègles, France
[c] PACEA, Université de Bordeaux – CNRS, bâtiment B18, allée Geoffroy-Saint-Hilaire, 33615 Pessac Cedex, France
[d] Laboratoire de Météorologie Dynamique/IPSL, Sorbonne Universités, UPMC Université Paris 06, ENS, PSL Research University, École Polytechnique, Université Paris Saclay, CNRS, Paris, France
[e] Bordeaux Sciences Agro, 1 cours du Général de Gaulle, CS 40201, 33175 Gradignan, France
[f] Laboratoire de Météorologie Dynamique/IPSL, Département de géosciences, ENS, PSL Research University, École Polytechnique, Université Paris Saclay, Sorbonne Universités, UPMC Université Paris 06, CNRS, Paris, France
[g] Lamont-Doherty Earth Observatory of Columbia University, Palisades, NY 10964, USA

ARTICLE INFO

Article history:
Received 18 April 2017
Received in revised form
21 June 2017
Accepted 28 June 2017

Keywords:
Coversand
Loess
Last glacial
Dunes
Grain-size modelling
Geochemistry
Wind direction
Southwest France

ABSTRACT

Dune pattern, grain-size gradients and geochemistry were used to investigate the sources and dynamics of aeolian deposition during the last glacial in southwest France. The coversands form widespread fields of low-amplitude ridges (zibars), whereas Younger Dryas parabolic dunes mainly concentrate in corridors and along rivers. Spatial modelling of grain-size gradients combined with geochemical analysis points to a genetic relationship between coversands and loess, the latter resulting primarily from dust produced by aeolian abrasion of the coversands. The alluvium of the Garonne river provided also significant amounts of dust at a more local scale. The geochemical composition of loess shows much lower scattering than that of coversands, due to stronger homogenisation during transport in the atmosphere. Overall, sandy loess and loess deposits decrease in thickness away from the coversands. Dune orientation and grain-size gradients suggest that the efficient winds blew respectively from the W to the NW during the glacial, and the W-SW during the Younger Dryas. A comparison between the wind directions derived from the proxy data and those provided by palaeoclimatic simulations suggests a change of the main transport season. Ground surface conditions and their evolution throughout the year, i.e. the length of the season with snow and frozen or moist topsoil, and the seasonal distribution of wind speeds able to cause deflation are thought to have been the main factors that controlled the transport season in the study area.

1. Introduction

In the Aquitaine basin (Southwest France), Pleistocene coversands spread over a surface of approximately 12,000 km^2, and are bordered on their eastern and southern margins by a large loess belt. The stratigraphy of aeolian deposits has been the focus of recent studies and a large set of ^{14}C, ESR and OSL ages is available both for coversands and loess (Bertran et al., 2009, 2011; Hernandez et al., 2012; Sitzia et al., 2015). Mapping of aeolian deposits has also been the subject of many attempts. The conventional field approach allowed precise delineation of the coversands since the 60's (Enjalbert, 1960; Legigan, 1979), but the loess deposits were always omitted in the maps, and are still lacking on the current 1/50,000 geological map of France (*infoterre.brgm.fr*). Bertran et al. (2011) showed the potential of coupling field mapping and the use of soil databases designed for agricultural purposes, in which physico-chemical analyses of topsoil samples are listed. A first map of loess and transitional facies was produced using the

* Corresponding author.
E-mail address: lcsitzia@gmail.com (L. Sitzia).

http://dx.doi.org/10.1016/j.quascirev.2017.06.029
0277-3791/

online BDAT database (www.gissol.fr) where the sand, silt and clay content of topsoil samples are averaged at the scale of administrative units of an area of tens of square kilometers. Since then, the Land Use and Cover Area frame Statistical survey (LUCAS) database on topsoil properties in Europe has been made available and was used for further mapping of aeolian deposits (Bertran et al., 2016). The points which satisfy the grain-size criteria of coversands and loess were extracted from the rasters of predicted soil texture established by kriging of the LUCAS data by Ballabio et al. (2016). These rasters have a resolution of 500 m. A comparison with previous maps showed a good fit in most of the tested areas in Europe (Bertran et al., 2016). Improvement of the French database (Donesol, http://acklins.orleans.inra.fr/outil/donesol) and access to raw data makes it now possible to investigate more in detail the aeolian deposits at a regional scale, since more refined information on grain-size composition and on loess thickness is available.

Pioneer mineralogical studies have been performed by Klingebiel (1966) and Legigan (1979). They have suggested that the sources of the coversands were mostly Mio-Pliocene alluvial and deltaic sands that crop out on the continental plateau. However, these studies remain crude, and the possible contribution of wind-blown particles derived from the alluvium fed by the surrounding ranges (Massif Central, Pyrenees) was hardly detectable using heavy mineral analyses alone. The provenance of the particles and the transport paths remain, therefore, to be documented in detail. Grain-size gradients (Lautridou, 1985; Ruegg, 1983; Liu, 1988), loess thickness (Frazee et al., 1970; Mason, 2001), and the mineralogical and chemical composition of the deposits (Muhs et al., 2008; Stevens et al., 2010; Rousseau et al., 2014) have proved to be efficient tools for reconstructing the transport paths at a regional scale and for identifying the main factors involved in deposition. Together with dune orientation, these data give insight into past atmospheric circulation and have been widely used for reconstructing wind directions during the Last Glacial in Europe (Poser, 1950; Maarleveld, 1960; Léger, 1990; Isarin et al., 1997; Zeeberg, 1998; Van Huissteden et al., 2001; Renssen et al., 2007).

The aim of this paper is to combined geomorphological, sedimentological and geochemical approaches to better understand the origin and dynamics of the aeolian deposition in southwest France. Then, the reconstructed wind regimes during the Last Glacial in the study area are compared with previous climatic simulations (Sima et al., 2009, 2013), in an attempt to identify the period of the year favourable to dust activity for different climate patterns.

2. Geological setting

Since the beginning of the Middle Pleistocene, the centre of the Aquitaine basin was quite similar to its current configuration and corresponded to a sand plain almost lacking relief and gently sloping toward the Atlantic Ocean. Such a context, unparalleled along the French coast, favoured the accumulation and preservation of aeolian deposits throughout the glacial phases of the Pleistocene (Bertran et al., 2011; Sitzia et al., 2015).

At the basin scale, the following geomorphological units have been distinguished (Fig. 1B): (1) ventifact pavements, present mainly in the northern part of the basin at the surface of the plateau alluvium on both sides of the Garonne River (Plateau Girondin and Blayais); (2) the coversands ("Sable des Landes Formation" *sensu* Sitzia et al., 2015), limited by the Garonne river to the east and the north, the Adour river to the south, and the Atlantic Ocean to the west; (3) a large loess belt mainly developed to the east and the south of the coversands.

Recent works allowed reappraisal of the regional chronostratigraphy of sand and loess deposits (Bertran et al., 2009, 2011; Sitzia et al., 2015). Three main phases of coversand

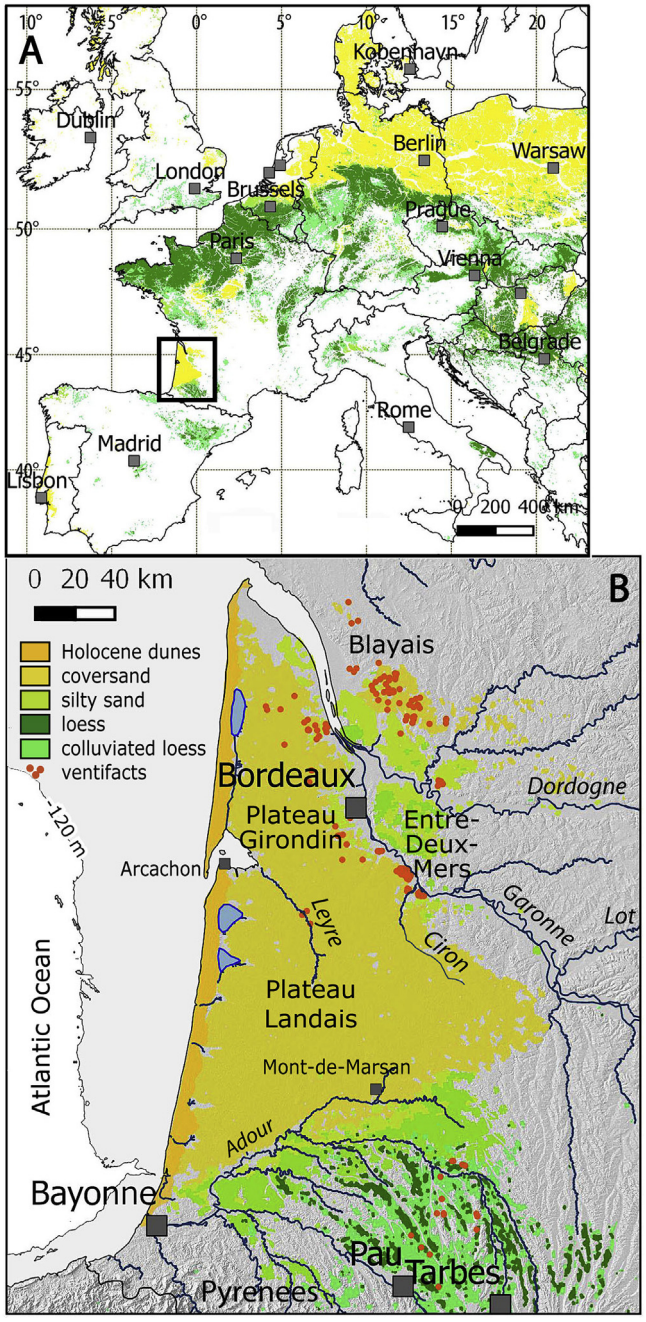

Fig. 1. European aeolian deposits. A – General map from Bertran et al. (2016) and location of the study area; B – Close-up view of southwest France. The distribution of ventifacts is from Bertran et al. (2011).

accumulation were identified throughout the Last Glacial (Sitzia et al., 2015): (1) Marine Isotopic Stage (MIS) 4–3 (64–32 ka), characterized by predominant wet sandsheet accumulation; (2) MIS 2 and the beginning of MIS 1 (Greenland Interstadial 1e) (25–14 ka), associated with the development of dry sandsheets and coincident with the maximum expansion of the Landes desert; (3) Younger Dryas (YD, Greenland Stadial 1), marked by the development of parabolic dune fields. Parabolic and dome dunes dating back to the 14th-19th centuries have also been documented and probably reflect local dune reactivation due to increased human impact on the vegetal cover during the Little Ice Age (Bertran et al., 2011).

Sitzia et al. (2015), through the analysis of the chronological data of near-surface coversands, revealed an uneven geographical distribution of the ages. They are dominantly Middle Pleistocene in the northernmost part, MIS 4–3 in the Plateau Girondin, and MIS 2 to YD in the Plateau Landais to the south. According to the authors, this pattern might have resulted from a deficit in sand in the north during the Last Glacial Maximum (LGM) since the emerged continental plateau was much wider (and as a consequence, the coastline was more distant) than in the south. Available ages for loess suggest that they accumulated mainly during the two last glacial periods (Bertran et al., 2011; Hernandez et al., 2012).

3. Modern wind regime

Prevailing winds along the Atlantic coast of mid-latitude Western Europe are handled by two major pressure areas, the Azores High, located in the Atlantic Ocean between latitude 25 and 40°N, and the Icelandic Low, located between latitude 60 and 75°N. Seasonally, the position of these two pressure centres shifts and the wind regime changes. During the winter, dominant winds come from the southeast, whereas westerly to northwesterly winds are the most prominent during the summer (Fig. 2A). The map of mean wind speeds at 10 m available at the European Joint Research Centre (http://agri4cast.jrc.ec.europa.eu/DataPortal) shows the following (Fig. 2B):

(1) The highest wind speeds are observed along the coast and in the Garonne estuary where channelling of the airflows leads to wind acceleration;
(2) Overall, the wind speeds decrease the further the altitude increases;
(3) The area with the lowest mean wind speed is located at the southern edge of the Pleistocene coversands.

4. Data and methods

4.1. Analysis of dune patterns

The pattern of the dune ridges has been analysed using (1) digitized black-and-white aerial photographs from the 1950 missions (1/25,000) of the French Institut Géographique National (IGN) and (2) IGN aerial colour photographs available on Google Earth. The main dune morphologies were described according to McKee (1979). To establish the crest direction we followed the approach proposed by Ewing et al. (2006). For barchanoid ridges, a line parallel to the general direction of the dune crest was used.

Most of the parabolic dunes have been mapped during the 1/50,000 geological survey of the Aquitaine basin by the French Bureau des Recherches Géologiques et Minières (BRGM) (Capdeville and Dubreuilh, 1994). The dune morphologies were described according to the terminology of Pye and Tsoar (2009), and the growth direction was measured using the bisector of the angle between the two arms of the dune.

Where available, the Digital Elevation Model (DEM) 5 m of the IGN (RGE Alti® 2.0, ©IGN, 2014) made it possible the observation of the detailed morphology of the parabolic dunes. Since the small aeolian ridges remain difficult to identify from the DEM, a photogrammetric survey has been performed with a drone in 3 areas of 1–8 km^2, which provided more precise elevation data. The pixel resolution is 0.3 m.

4.2. Grain size, thickness and geochemistry of the aeolian deposits

The grain size and thickness dataset consists of (1) data collected in this work or previously published (Bertran et al., 2009, 2011; Dubreuilh, 1976; Thibault, 1970), and (2) data available from the Donesol database (INRA, 2011) for the Gironde, Landes, Dordogne and Lot-et-Garonne districts. The datasets were cleaned to select only the outcrops and the stratigraphical units of aeolian origin. The selected data were finally treated for the purpose of geostatistical analysis.

The samples for grain-size analysis were processed in the PACEA laboratory (Université de Bordeaux) using a Horiba LA-950 laser particle size analyser. The sample pre-treatment includes suspension in sodium hexametaphosphate (5 g/L) and hydrogen peroxide (35%) for 12 h, and 60 s of ultrasonification in the analyser to achieve optimal dispersion. The Mie solution to Maxwell's equations provided the basis for calculating the particle size as is recommended by the ISO committee (Jones, 2003; ISO, 2009), using a refractive index of 1333 for water and 1.55i - 0.01i for the particles (see Supplementary Information 2). In the Donesol database, the grain-size limits are those used by the French pedologists (Duchaufour, 1997), i.e. 2000–200 μm (coarse sand), 200–50 μm (fine sand); 50–20 μm (coarse silt); 20–2 μm (fine silt); <2 μm (clay). The analyses used in the database have been done by wet

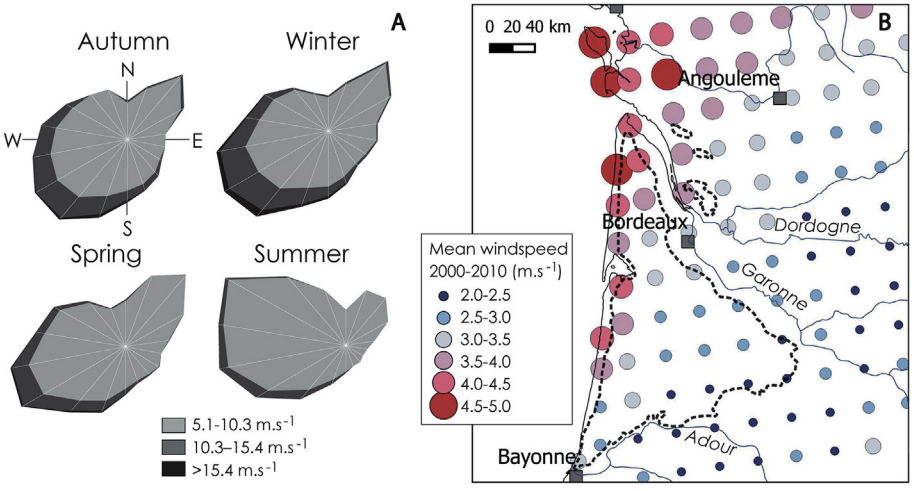

Fig. 2. Modern meteorological parameters in the studied area. A - Roses of seasonal winds in Aquitaine (period 1999–2007) according to MétéoFrance (Ile d'Yeu weather station); B - Mean wind speeds (m.s^{-1}) at a height of 80 m, from Agri4cast (2016); the dashed line indicates the coversand limit.

sieving of the particles >50 μm and with the pipette method for the particles <50 μm. The results obtained with this method cannot be directly compared with those obtained with the laser particle size analyser (Konert and Vandenberghe, 1997; Buurman et al., 2001; Antoine et al., 2001). Here, after comparing 20 samples treated using both methods, the following limit classes have been chosen: <4.6 μm (clays), 4.6–26 μm (fine silt), 26–50 μm (coarse silt), >50 μm (sand). These limits are similar to those used by Antoine et al. (2001). Polymodal grain size distributions expressed in phi units have been deconvoluted in populations of particles characterized by a Gaussian distribution using the software Fityk 0.9.8 (Wojdyr, 2010) to identify precisely the main modes and to follow their spatial evolution.

The samples selected for the geochemical analysis (n = 77) come from outcrops studied during this work or previously published (Bertran et al., 2009, 2011; Sitzia et al., 2015). The outcrops have been selected in order to characterize the main types of aeolian deposits and their potential sources: (1) Last Glacial coversands n = 22); (2) YD parabolic dunes (n = 13); (3) loess from the Landes area (n = 17); (4) loess from the Entre-Deux-Mers area (n = 4); (5) recent alluvium of the Leyre (n = 4), the Ciron (n = 3), the Garonne (n = 3) and the Adour (n = 3) rivers; (6) Plio-Pleistocene plateau alluvial deposits (n = 7). The samples from aeolian sands have been taken below the B horizon of the surface podzol. All the loess samples come from the argillic Bt horizon and were taken between 0.6 and 0.9 m deep. After removing the grains >2 mm, the sand fraction was separated from the component <63 μm by wet sieving and crushed. The sand and the fine fractions have been analysed apart by Energy Dispersive X-Ray Fluorescence (ED-XRF) by the spectrometry division of Ametek (Elancourt, France). The measurements were made with a XEPOS instrument and do not allow quantification of elements lighter than aluminum. Quantification was based on fundamental parameters.

Some representative samples of aeolian deposits and possible sources have been studied by X-Ray Diffraction (XRD). As for ED-XRF, the sand and silt/clay fractions were studied separately. The analysis was carried out by the Institut de Chimie de la Matière Condensée in Bordeaux (ICMCB) using a PANalytical X'Pert diffractometer with a Bragg - Brentano theta – theta configuration. The measurements were made with a measuring time of 30 mn, between 8 and 80° and with a minimum step angle of 0.02°. Mineralogical identification was performed using the EVA software coupled with a JCPDS-ICDD PDF2 database.

The grain-size and the geochemical data are expressed as percentages; therefore, they have to be considered as compositional data (Aitchison, 1982). The analysis of compositional data by classic multivariate statistics provides inappropriate results (Aitchison, 1982). Aitchison (1986) proposed a robust solution to this problem, which used the logarithms of component ratios instead of the raw percentages. In this work, because of the nature of the data, we used non parametric replacement of the null values according to the method proposed by Martín-Fernández et al. (2003) for below-detection values. Here, all the compositional data were analysed using the CoDaPack software (Comas-Cufí and Thió-Henestrosa, 2011).

For the purpose of geostatistical data analysis, a variographic analysis (Webster and Oliver, 2007) has been carried out with the VarioWin software (Pannatier, 1996). For compositional data, in agreement with Pawlowsky and Burger (1992), each variable was transformed before variographic analysis. Here, the Isometric Logratio Transformation has been applied (Egozcue et al., 2003). Finally, we used ordinary kriging (Webster and Oliver, 2007) for the interpolation through the geostatistical toolbox of ArcGis 9.3.

The models obtained have been tested by a double cross validation. In ArcGis, the value of a variable is estimated in each point of the space by kriging and this operation is repeated every time by removing one of the points for which the true value was originally known. Following this procedure, the software calculates the mean error (ME) and the mean square deviation ratio (MSDR). The mean error has to be close to 0, while the mean squared deviation ratio has be as close as possible to 1 (Webster and Oliver, 2007). The model validity has been also measured through an independent data set. The original database (grain size, thickness) selected for the geostatistical analysis has been split before the variographic analysis using the random selection spatial tool of ArcGis. We chose to randomly select 10% of the total number of samples. The remaining 90% have then been used for the variographic analysis and the calculation of the ME and MSDR statistics. Doing so, it was possible to plot the observed values (independent data set) against the estimated values and to calculate a linear regression between the two sets. Following Pawlowsky-Glahn and Olea (2004), the fitness of the regression for grain-size data was evaluated by calculating the standardized residual sum of squares (STRESS). The closer the value of the STRESS index to zero, the less is the difference between observed and estimated values, and thus the best is the tested modelling.

4.3. High-resolution glacial climate simulations

We dispose of two numerical palaeoclimatic simulations at high-resolution over the studied area that we can compare to our proxy data. The first simulation, designed for the Last Glacial Maximum (LGM), was used by Banks et al. (2009) for niche modelling. In this simulation, the orbital parameters and the atmospheric CO_2 concentration (Berger, 1978; Raynaud et al., 1993) were set to their values for 21 ka. The LGM ice-sheet configuration (height and extent) reconstructed by Peltier (2004, ICE-5G) was prescribed, and the land-sea mask was adjusted to a sea-level drop of about 120 m. The GLAMAP2000 reconstruction of the LGM sea-surface temperatures (SSTs) and sea-ice extent was imposed (Paul and Schäfer-Neth, 2003; Sarnthein et al., 2003). The second simulation is one of the numerical experiments used by Sima et al. (2009, 2013) to study the European climate (and dust) sensitivity to changes in North-Atlantic SSTs as those associated with the MIS 3 millennial-timescale variability. The orbital parameters and CO_2 concentration are set to 39 ka values, the ice-sheet configuration, also selected from the ICE-5G reconstructions, corresponds to a sea level about 60 m lower than today (i.e. half of the LGM value), and the land-sea mask is adapted to the sea-level drop. Because no reconstruction or modelling result was available at that time for MIS 3 sea-surface conditions, the GLAMAP2000 dataset was imposed in the base-line MIS 3 simulation. A cold and a warm perturbation were obtained by applying zonal anomalies of up to 2 °C to the GLAMAP North-Atlantic SSTs in the latitudinal band between 30°N and 63°N. Considering the differences of North-Atlantic SSTs between the LGM and an average MIS 3 state suggested by experiments with an earth system model of intermediate complexity (van Meerbeeck et al., 2009), here we use the warm perturbation (hereafter “MIS 3” simulation) to characterize the average MIS 3 conditions in the comparison with the LGM.

In both MIS 3 and LGM experiments, the modern vegetation cover was prescribed in most regions, following the PMIP recommendations (e.g. Braconnot, 2004). Thus, in the area of interest here, trees occupy 60–80% of every grid-point in the coversands (in yellow on Fig. 1B), and about 15–40% elsewhere. The soil is bare all year long on 5–15% of the grid-points' surface, and the rest up to 100% of each grid-point is occupied by grass. This is a drawback because the LGM vegetation was much scarcer. The use of modern vegetation most probably does not affect the simulated wind direction, but it does affect the wind speed, which is strongly reduced

due to overestimating the roughness length. As the wind speed is a key element in determining the season(s) when dust emissions occur, we also present sensitivity tests of this variable to more appropriate values of roughness length. Using prescribed present-day vegetation also leads to unrealistically overestimating its effect of protecting the ground from aeolian erosion. Thus, for the impact of the surface conditions on the dusty season, we will only be able to discuss soil moisture and snow cover.

The simulations were performed with the LMDZ atmospheric general circulation model (version 3.3), coupled with the SECHIBA land surface model (Krinner et al., 2005), on a stretched grid with resolution down to 60 km on Western Europe. For each simulation there are 21 years of run, one year of spin-up followed by 20 years for analyses.

5. Results

5.1. Dunes

5.1.1. Low amplitude dunes

Among the low amplitude dunes, four main morphological types have been identified from aerial photographs: transverse ridges, barchanoid ridges, isolated barchanoid ridges and dome dunes/sand patches. The ridges appear in cultivated areas as bright lineaments separated by darker interdune areas due to variations in soil organic and water content. Most of the ridge fields were observed in the Plateau Girondin area, where the groundwater table is close to the ground surface and the YD parabolic dunes are scarce. According to available chronological data, these ridges date back to MIS 4–3, or possibly to older phases of sand deposition in the northernmost area. The DEM provided by photogrammetry shows that the ridge pattern corresponds to regular to irregular low amplitude reliefs, 0.3–0.7 m high and 70–150 m in wavelength (Fig. 3). The reliefs are aligned along the bright lineaments visible in aerial photographs. In contrast, no significant ridge areas were found in aerial photographs to the south on the Plateau Landais where the MIS 2 coversands are thicker. Field survey, however, showed that ridges also were present there in small areas forming well-preserved linear reliefs approximately 1 m in height (Fig. 4). In cross-sections, all these dune-like forms are associated to a sand-sheet facies; high-angle stratification is almost absent (Sitzia et al., 2015).

In the Plateau Girondin, the following observations can be made (Fig. 5): (1) the different types of ridge morphologies form homogeneous fields elongated parallel to the coast; (2) the dome dunes/sand patches are located on the margins of the barchanoid and transverse ridge fields; (3) the dune fields are replaced toward the east by an area characterized by thin sandsheet deposits almost lacking dune-like forms; (4) the distribution of the different types of morphologies seems to be mainly controlled by topography.

A total of 425 measurements of crest direction have been made from barchanoid and transverse ridges. The rose diagrams show that predominant crest directions are consistently N-S (i.e. the vector perpendicular to dune crests is W-E, Fig. 5A). Local departure from this direction was found to be mainly controlled by topography. This is particularly obvious in Fig. 5C for the transverse ridges whose crest direction, roughly parallel to the contour lines, vary between N-S and NE-SW within a few kilometres.

5.1.2. Parabolic dunes

The parabolic dunes are 10–15 m high and exceptionally exceed 25 m (Dune de Cazalis, Legigan, 1979). The total number of digitized dunes is 2636. Following the typology proposed by Pye and Tsoar (2009), simple (hairpin, lunate), complex (hemicyclic, digitated, nested, rake-like, en-echelon) and compound (long-walled ridge with secondary transverse arms) forms were observed.

The parabolic dunes exhibit a non-random distribution over the landscape. They are mainly clustered around the rivers, and form corridors up to 80 km in length along shallow valleys oriented W-E and over the plateau (Fig. 6). The dune morphology changes according to topography. Along the Leyre and the Ciron valleys, as well as near the coast, the parabolic dunes are mostly simple; on the contrary, complex and compound forms are mainly observed in the corridors (Fig. 7A, C). Complex forms several kilometres in length have been observed in the main dune corridor (Fig. 7B).

A total of 394 measurements of dune orientation have been made. The rose diagrams reveal a systematic orientation towards the ENE and a low dispersion of the values (Fig. 6).

5.2. Grain-size gradients at the basin scale

In the Donesol grain-size database, 513 out of the 3683 sites, considered to be pure (i.e. non colluviated) aeolian deposits, were retained (Fig. 8). Among the selected sites, 462 were used in the geostatistical analysis and 51 for cross-validation. The results of cross-validation (see Supplementary Information) indicate that both the variographic analysis and the ordinary kriging were satisfactory. The interpolated maps of the content in coarse sand, fine sand, coarse silt and fine silt are shown in Fig. 8. The following observations can be made: (1) every grain-size class shows a gradient oriented NW-SE; (2) the coarse fractions are mainly located in the north-western part of the basin and extend inland from Arcachon to the SE; (3) the Garonne and Adour valleys (and their tributaries) serve as limits for the coversands; the silty sand facies are restricted to a narrow strip on the left bank of the Garonne river, whereas they form a broader band on the right bank and in the southern part of the basin; (4) in the loess belt, the ratio coarse/fine silt varies only slightly in the study area. When increasing the number of grain-size classes, it can be observed that, both in the Entre-Deux-Mers area and in the southern part of the basin, the coarse silt maximum is located northwest of the fine silt maximum (Fig. 9). Comparison between these maps and that derived from the LUCAS database (Fig. 1) shows that loess have a more limited extent in the latter, where the mapped aeolian units have, therefore, to be considered as minimal.

The sand deposits extend up to the border of the Landes plateau and show a main mode ranging between 340 μm for the northernmost site (Retjons) and 270 μm for the southernmost one (Pujole-Plan) (Fig. 10B). In the Adour valley and its tributaries, the distribution is polymodal. From the north to the south, the main mode is first in medium sands (270 μm) and then decreases rapidly and gives way to a mode on silts (22 μm). In this area it can be noticed (1) a rapid decrease in the size of the sand particles (Fig. 10B); (2) a decrease in the contribution of the coarse modes in favour of the finer modes (Fig. 10C). Finally, south to the Adour valley, a mode around 17 μm becomes predominant (Fig. 11A). This mode decreases from 17 to 14 μm quite evenly as a function of the distance to the coversands. For all the sites located between the Adour valley and the Pyrenean foothills, significant amounts of clay are present. The mode, close to 3 μm, remains steady regardless of the distance to the coversands (Fig. 11A), whereas the total clay content slowly increases with distance (Fig. 10D).

In the northern part of the basin, the grain-size distributions show that (1) the sands of the Blayais area are relatively coarse (mode between 300 and 600 μm); (2) the silts of the Entre-Deux-Mers area have a mode between 30 and 34 μm; this is appreciably coarser than the mode of the loess deposits in the southern part of the basin; (3) the silt mode decreases significantly toward the SE. The most distant sample from the sources (Barbas) has a mode around 12 μm.

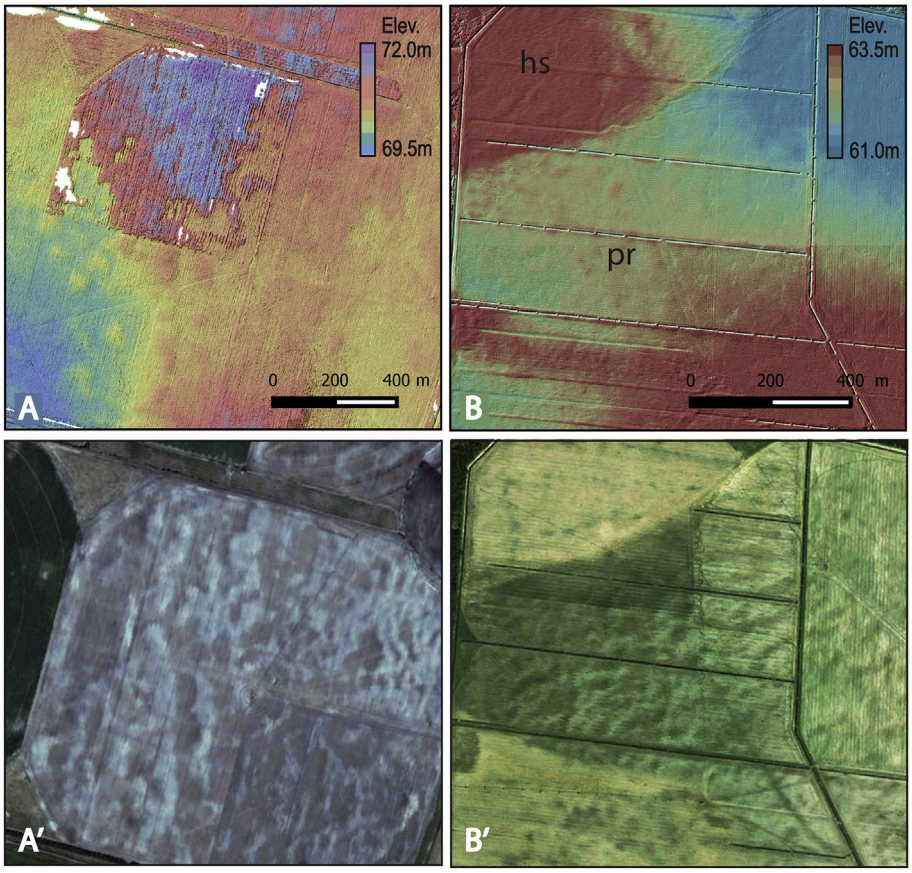

Fig. 3. A, B - Detailed topography of barchanoid ridges (photogrammetry); location shown in Fig. 4A pr – Pleistocene ridge field; hs: Holocene sand cover at the front of a parabolic dune. North to the top. A′, B' – Aerial views of the same areas (photos IGN/Google Earth).

Fig. 4. View of transverse ridges dated to MIS 2, Pontonx-sur-l'Adour.

5.3. Thickness variability at the basin scale

According to Karnay et al. (2010), the coversands (Sable des Landes Formation) form a thin sheet, usually less than 2–3 m thick. Nevertheless, the underlying Castet Formation (Dubreuilh et al., 1995), which is now considered to be part of the Sable des Landes Formation (Sitzia et al., 2015) and reaches locally up to 40 m in thickness, was not considered by Karnay et al. (2010). As a whole, the coversand thickness decreases from the west to the east according to the distance to the coast and with altitude.

The loess data were partitioned in two sets, one for the north (n = 292), and the other for the south (n = 434). The geostatistical analysis points out that (1) the ordinary kriging decreases systematically the standard deviation of the thickness around the mean; (2) the deviation between measured and estimated values is larger for the northern data set. The Anderson-Darling test reveals that the deviation distribution fits a normal (Gaussian) distribution. For the southern loess, the accuracy of thickness estimation is 57.4 cm and the mean error is 81.8 cm. The most significant errors are due to extreme values. For the northern loess, the accuracy of estimation and the mean error cannot be evaluated because the deviation distribution does not follow a Gaussian function.

The interpolated maps show that the loess thickness decreases rapidly with increasing distance to the coversands, in a gradual way in the southern area, more steeply in the northern area (Fig. 12). The maximum loess thickness reaches 3.5 m in the south and 5 m in the north. Because of the uneven distribution of the selected Donesol data and the loose geographical coverage, the interpolated maps do not make it possible to identify if deposition preferentially occurred on particular slopes according to their orientation.

5.4. Geochemistry and potential sources

The distribution maps of elemental compositions (Fig. 13) and the scattergrams of the elements versus Si (Fig. 14) (mainly as quartz) point out the following:

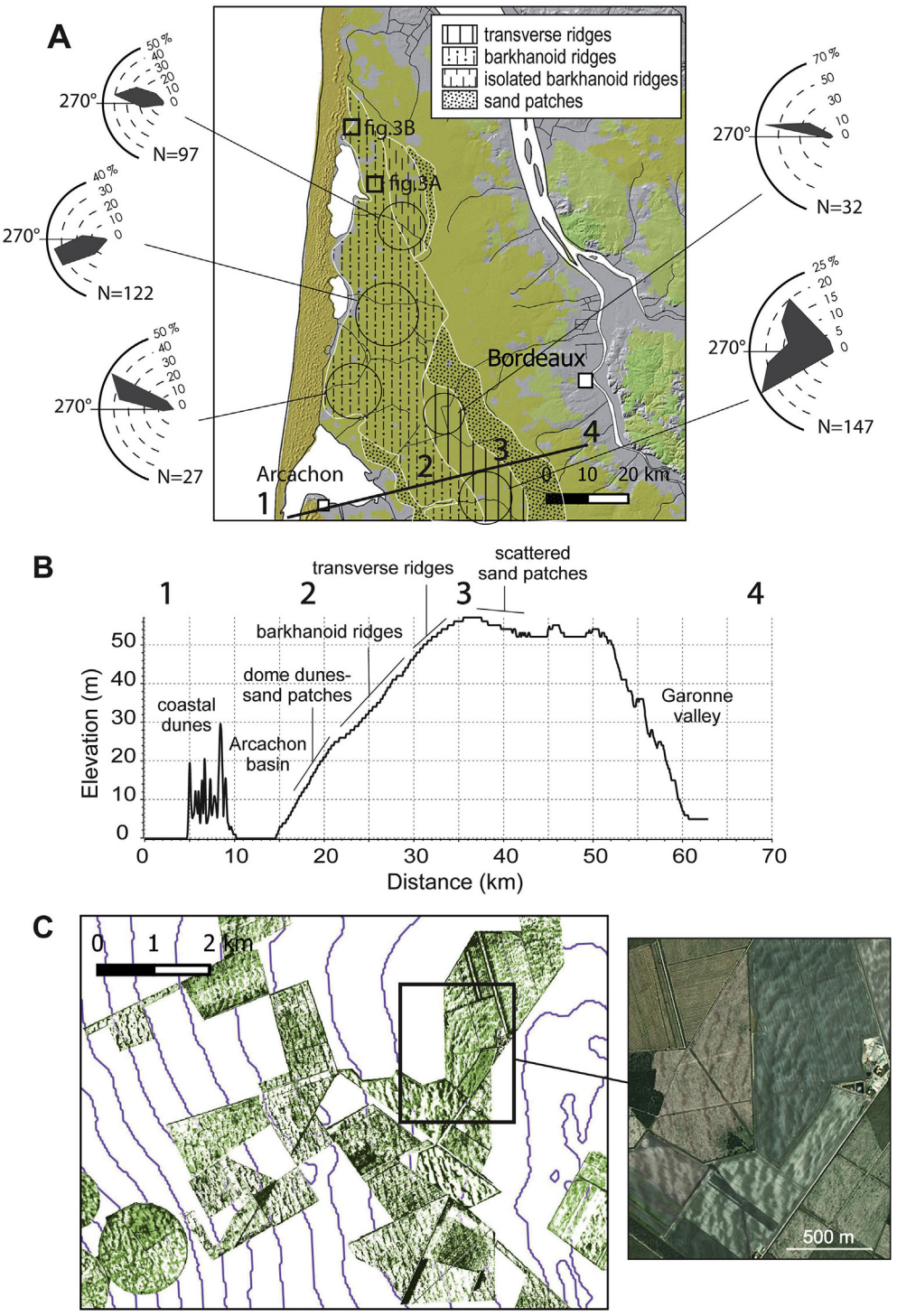

Fig. 5. Ridges of the Plateau Girondin. A – Distribution of low-amplitude ridges (zibars) and orientation of the vector perpendicular to dune crests. B – Topographic transect between the Atlantic coast and the Garonne river, and associated dunes morphologies. C – Photo-mosaic of fields showing low-amplitude ridges (photos IGN/Google Earth) with superimposed 5 m contour lines, and close-up view of ridge fields.

(1) Zr, the principal component of zircon, and Ti, probably as oxides, are mainly concentrated in the fine fraction (silt, fine sand). Therefore, these elements are mostly abundant in loess and in the fine fraction of the coversands. In a Si-Ti diagram, the samples of aeolian deposits are aligned along a line with a negative slope (Fig. 14, line a), except for the fine fraction of some coversand samples. This strongly suggests that the most of the aeolian samples result from the size fractionation of a common source of intermediate composition between that of sand and that of fines (Fralick and Kronberg, 1997). The samples from the Adour and Garonne rivers also show a linear trend (line b), but plot on a different line from that of the aeolian deposits, which indicates different sources. On the contrary, the samples from the

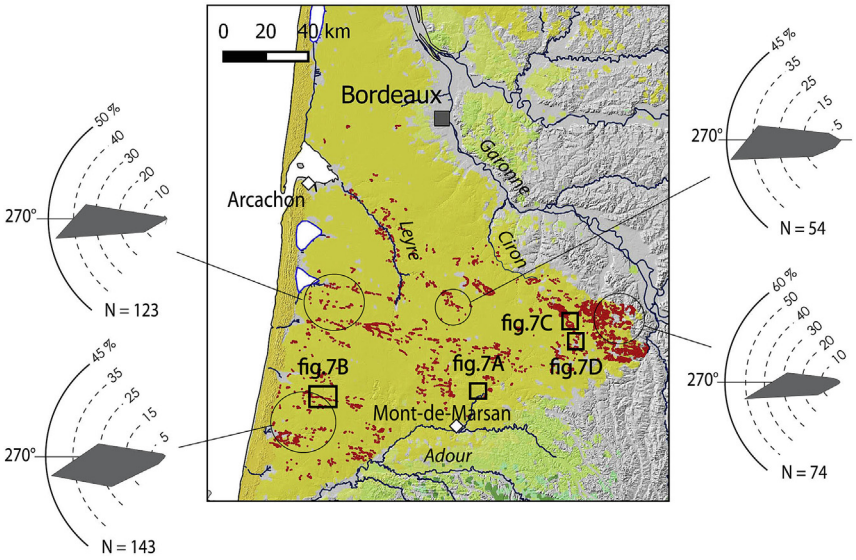

Fig. 6. Distribution of parabolic dunes (in red) according to the 1:50,000 geologic map (Bureau des Recherches Géologiques et Minières) and orientation of the bisector of the angle between the two arms for simple and complex dunes. The rectangles indicate the location of Fig. 6A–D. (For interpretation of the references to colour in this figure legend, the reader is referred to the web version of this article.)

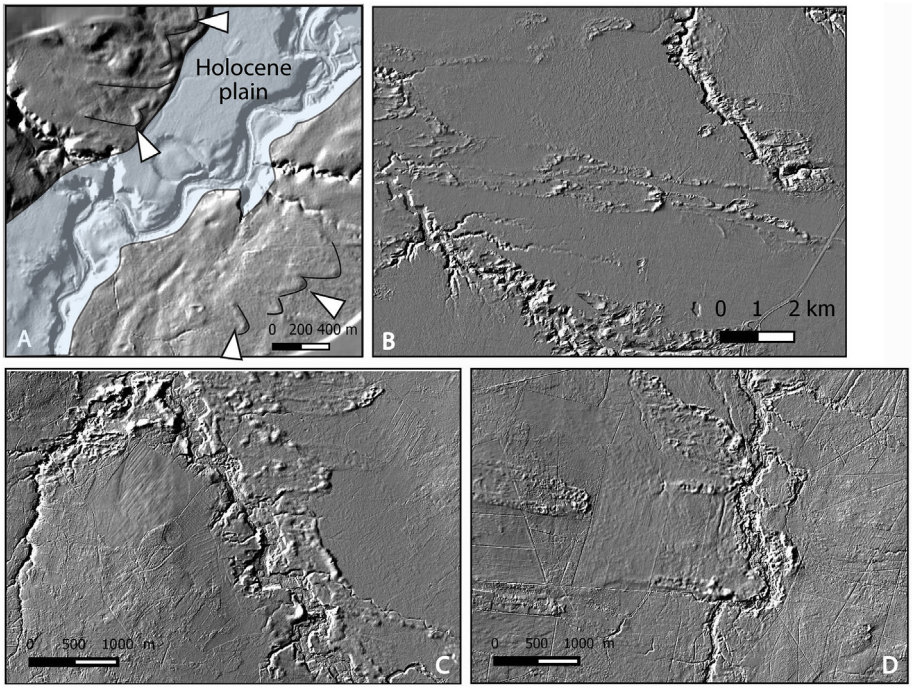

Fig. 7. Parabolic dunes, 5 m DEM (RGE Alti® 2.0, IGN, 2014). The areas represented are shown in Fig. 5 A – Dunes (indicated by white arrows) on both left and right banks of a river; B – Compound elongated parabolic dune; C - Parabolic dunes on the right (i.e. wind-facing) bank of a river; D - Dunes on the left bank of a river.

Leyre and the Ciron rivers, which drain both the coversands and old alluvial deposits, plot among the aeolian samples or between the Adour-Garonne and loess samples. Zr has a behaviour roughly similar to Ti. The loess composition appears to be homogeneous when compared with the whole data set. Such an observation is also valid for all the elements.

(2) Ca, as a component of carbonate or silicate minerals (feldspar, amphibole), is lacking in the aeolian sand fraction, whereas it has been found in small amount in the alluvial deposits. Ca has been detected as traces in the fine fraction of a few coversand samples where it is probably associated with Al in silicate minerals.

(3) K is present both in the aeolian sand fraction as part of silicate minerals (feldspar, muscovite) and in slightly larger amounts in the fine fraction (illite, mixed-layer illitic clay). Mean concentrations are significantly greater in the alluvial deposits. In the Si-K diagram, the K content of the aeolian sand fraction appears to be uncorrelated to Si and the samples are aligned on a horizontal line. On average, the sand fraction of loess is depleted in K in comparison with the

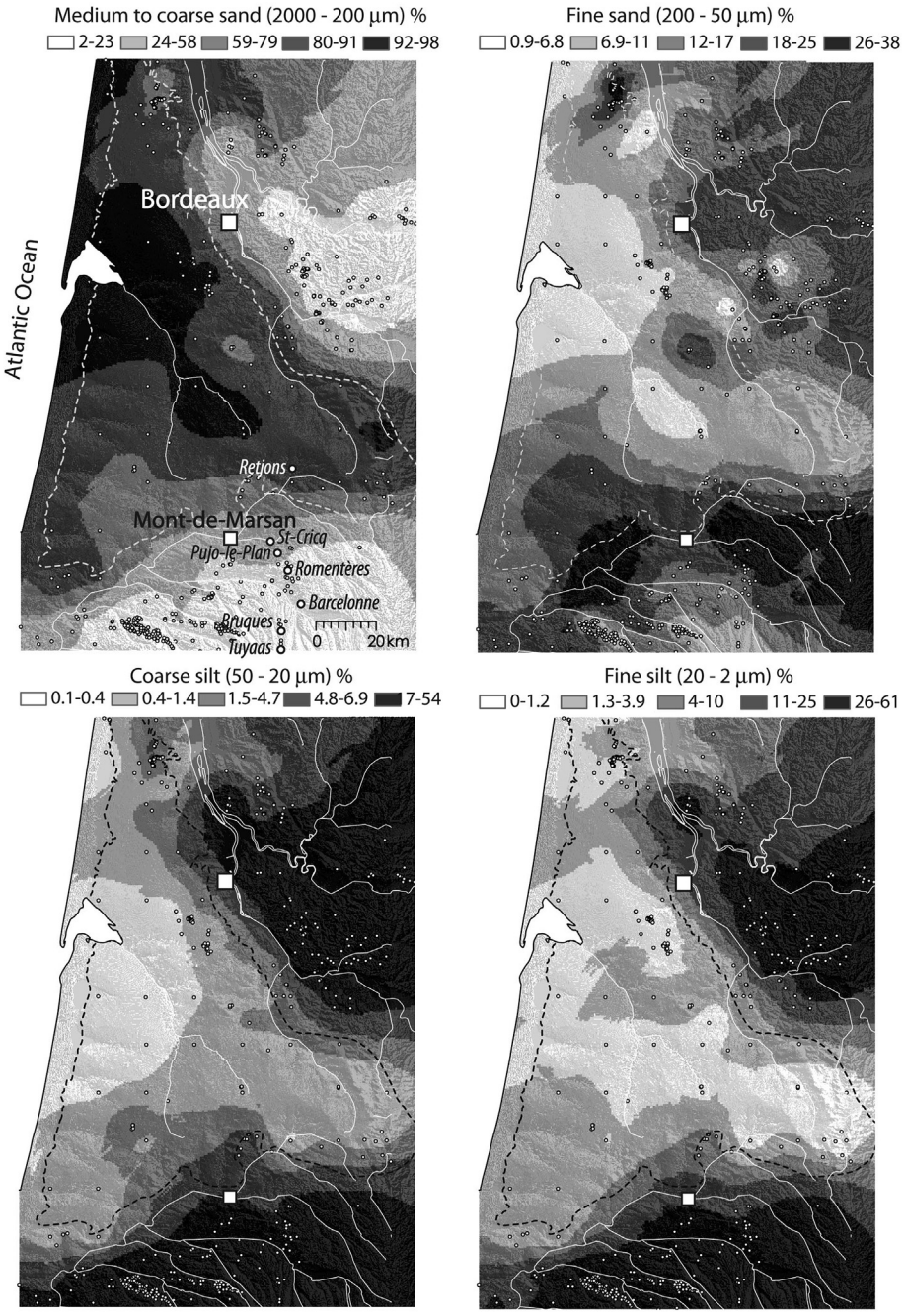

Fig. 8. Grain-size maps of the aeolian deposits interpolated by ordinary kriging. The white dots correspond to the sites used for kriging. The dotted line indicates the coversand limit.

coversands. The samples of fine fraction do not plot on the same line as the sands, but below it, suggesting a loss of K due to alteration and soil leaching (Fralick and Kronberg, 1997).

(4) On the Si-Al diagram (Fig. 14), the alignment of the aeolian samples along the same line suggests a partition of Al between sand and fines due to sedimentary sorting, with Al mainly concentrated in clays. High Al contents plotting above this line have been found only in the fine fraction of the coversands. Such enrichment in Al can be related to organic-mineral complexes in the B horizon of the surface podzol (Righi and De Coninck, 1974; Melkerud et al., 2000).

The principal component analysis ("compositional biplot", Aitchison and Greenacre, 2002) for the sand fraction (Fig. 15) explains 72.3% of the total variance. The first axis discriminates the group Ca + K + Rb + Sr from the group Fe + Ti + Zr. K and Rb are mainly related to K-silicates, mostly feldspar and micas (De Vos et al., 2006; Wedepohl, 1978). Sr has a size intermediate between K and Ca and can replace these two elements both in silicates and in carbonate minerals (De Vos et al., 2006). Because of the lack of carbonates in the studied samples, the group K + Rb + Sr reflects the pole of potassium silicates, while Ca corresponds to calcium silicates. Fe (+Cr as a substitute) is present in silicate minerals and in oxides and hydroxides (De Vos et al.,

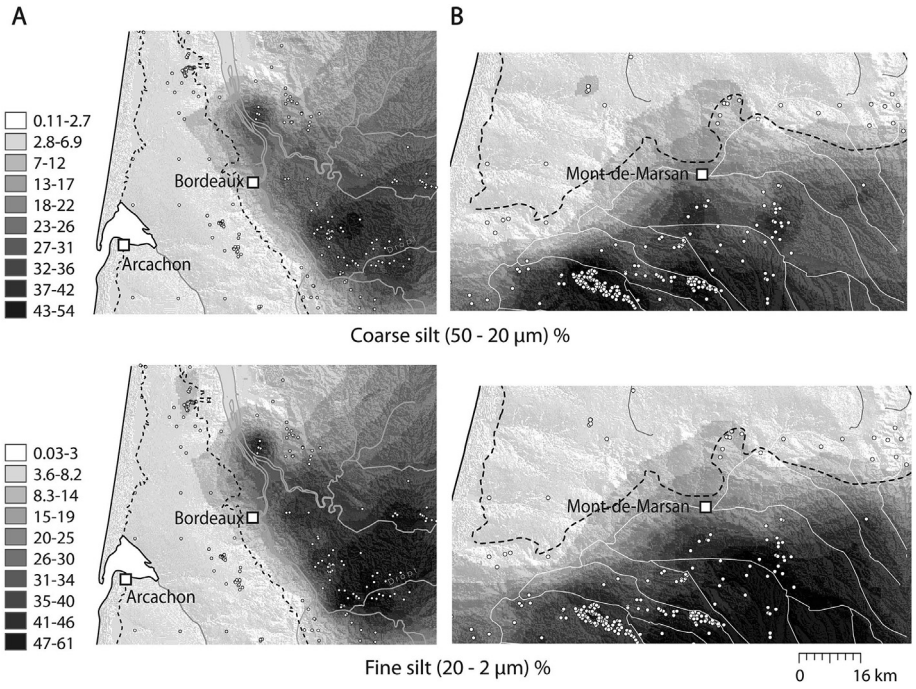

Fig. 9. Detailed maps of the coarse (upper panel) and fine (bottom panel) silt content in the northern (A) and the southern (B) part of the Aquitaine basin.

2006). The group Fe, Ti and Zr thus represents the pole of oxides and the minerals resistant to alteration.

The position of the samples in the biplot allows making the following remarks: (1) the samples of aeolian sands (Landes, Blayais, parabolic_dunes), the old alluvial terraces of the Garonne river (Plateau_alluvium), the recent alluvial deposits (Fz) of the Midou and Leyre rivers (which essentially drain the Sable des Landes Formation) are distributed between the barycentre of the biplot and the pole quartz + K-silicates; (2) the sand fraction of the southern loess (Loess_Landes) is associated with the pole of resistant minerals and oxides; (3) the recent alluvial deposits (Fz) of the Adour and Garonne rivers, which drain the Pyrenees, plot apart from the other samples, and are opposed to the pole quartz + resistant minerals; they include a high proportion of easily alterable Ca-minerals; (4) the sand fraction of the loess from the Entre-Deux-Mers area is located between the southern loess and the recent alluvial deposits.

The biplot for the fine fraction (Fig. 16), which takes into account a larger set of elements because of values above the detection limit, produces results substantially different from those for the sand fraction. It explains 63.7% of the total variance. Several poles can be distinguished. The first correspond to calcium-rich minerals (Ca); the second to resistant minerals, quartz and zircon (Si + Zr + Hf); the third to potassium silicates (K + Rb, and Ba, strongly adsorbed by soil clays, Reimann et al., 2014); and finally, the poles of Fe-oxides (Fe + Cr + As) and of Al-complexes (Al).

In this biplot, the loess samples appear more homogeneous and plot in the proximity of the pole oxides and K-silicates (probably dominated by clays). The loess composition partially covers that of coversands and is located apart of the recent alluvial deposits, which are close to the pole of Ca-minerals.

5.5. Results of climate simulations

Fig. 17 shows the results of the LGM and MIS 3 simulations for wind direction and for the variables that constrain the period of the year when dust emissions can occur, i.e. daily maximum wind speed (more informative for dust mobilization than daily average), snow-free surface fraction, and dry soil depth. The annual cycle of these variables is constructed on daily data for winds, and on monthly data for surface conditions, averaged over 20 years of run for each climate state and over the domain between longitude 2°W-1°E and latitude 43°-45.5°N (delimited by the black rectangle in Fig. 1A and zoomed in Fig. 1B).

The annual cycle of wind direction (Fig. 17A and B) is similar in the two simulations and not much different from the present-day one (Fig. 2). In both cases, the winds blow from W-SW in winter, turn from W in springtime, then from W-NW in summer. A reverse evolution occurs from the summer to the winter, through westerly winds in autumn. The daily maximum wind speed, averaged over the domain and over 20 years of run (black curves in Fig. 17C and D), is highest in winter, lowest in summer, and springtime values are higher than autumn ones. The LGM daily maximum winds are generally stronger than for MIS 3, especially from mid-May to October. The differences are small, and the values themselves are relatively low, less than 7 m s^{-1}. When looking at the highest (winter) daily maximum winds over all the individual grid cells and individual days of the 7200-point time series (i.e., 20 years × 360 days/year of run on a 360-day calendar), the values are often above 12 m s^{-1} in the MIS 3 run, with peaks at about 16 m s^{-1}, while in the LGM simulation the daily maximum winter values are frequently above 16 m s^{-1}, with extremes in excess of 20 m s^{-1}. The averages being comparatively quite low indicate however that these maxima represent local and rather brief intensifications. Even if the corresponding (winter) surface conditions (discussed later) allowed them to produce dust mobilization, this wouldn't match the strong dust activity suggested by the field data. The fact that the simulated winds are overall too weak is due to the high values of the roughness length ($z0$) calculated by the model on the basis of the present-day vegetation cover that was prescribed in both simulations. For comparison, z0 is about 37 cm on average on the studied domain, while values of 1 cm are associated in the model to bare soil. The vegetation was considerably scarcer than today for both LGM and average MIS 3 climates, so we

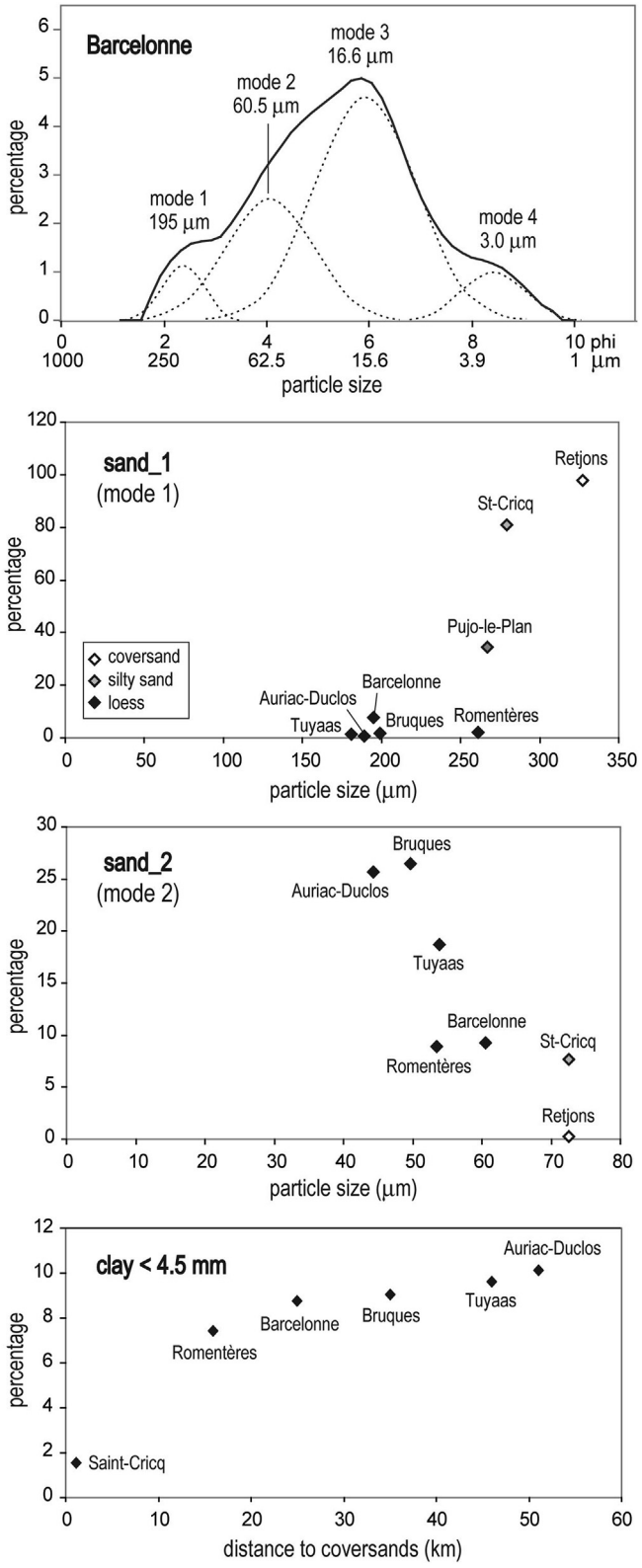

Fig. 10. Evolution of the grain-size mode of some representative samples from the southern part of the basin. The modes were established after deconvolution of the grain-size curves using the software Fityk 0.9.8 (Wojdyr, 2010). The location of the samples is shown in Fig. 8.

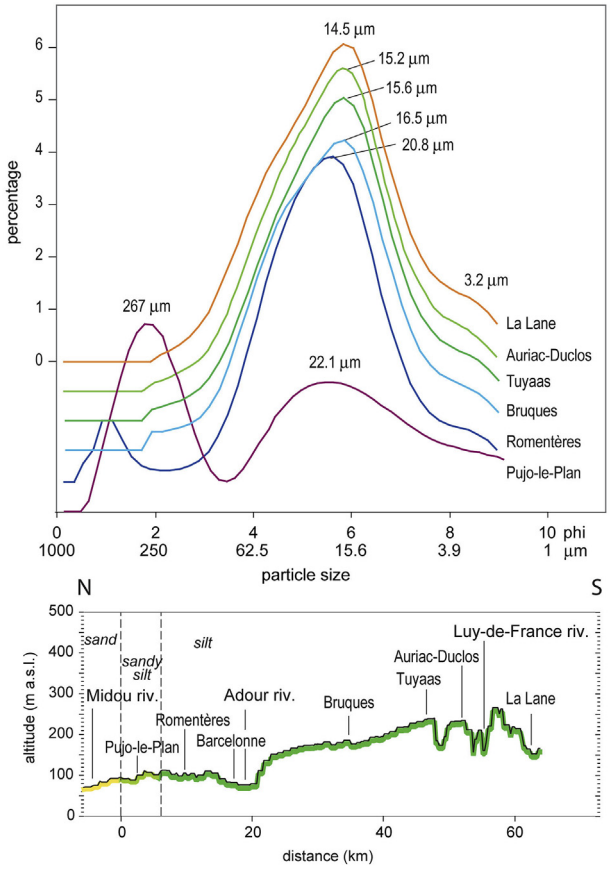

Fig. 11. Grain size distribution of some representative samples of sandy silts and loess from the Landes district. The location of the samples is shown in Fig. 8.

recalculate and plot the daily maximum winds for two values of z0 more adapted to the investigated area and periods. The blue curves in Fig. 17C and D correspond to z0 = 1.5 cm, and the green ones to z0 = 4 cm. The first z0 value is the one that the model would calculate for a surface covered by about 50% of grass, and the rest of bare soil. The second one corresponds to a majority of grass, with less than 10% bare soil and less than 10% trees (that can be assimilated to shrubs, which are not represented in the model). With these lower z0, the averages of daily maximum wind increase considerably, they almost double for z0 = 1.5 cm. Looking at individual days and grid cells, even for the relatively less windy MIS 3 and the higher test value z0 = 4 cm, the maximum daily values regularly exceed 25 m s^{-1} in winter, with a few peaks around 40 m s^{-1}. For z0 = 1.5 cm, the maximum winds over the domain are often around 30 m s^{-1} in winter, with peaks around 45 m s^{-1}.

Ahn et al. (2007) have statistically determined a wind-speed threshold of 7.5 m s^{-1} for dust mobilization in sandy areas from Asian deserts. If we consider this limit to also apply to the Landes coversands, the LGM average maximum winds practically never drop below it in the test with z0 = 1.5 cm, so that only the surface conditions would determine the dusty part of the year. For the MIS 3 run, the average daily maximum winds drop below the threshold in July for z0 = 1.5 cm, at mid-May for z0 = 4 cm respectively, and strengthen again in November in both tests. The tests with these z0 values can be interpreted in two ways. When comparing LGM to MIS 3, using the spatial averages of variables over the entire domain, the blue curve for the lower z0 (for about 50% grass and 50% bare soil) is more appropriate to characterize the LGM, and the green curve for the higher z0 (majority of grass, with some shrubs and bare soil) is more appropriate for a MIS 3 situation (so in Fig. 17C and D we plot these two more representative curves

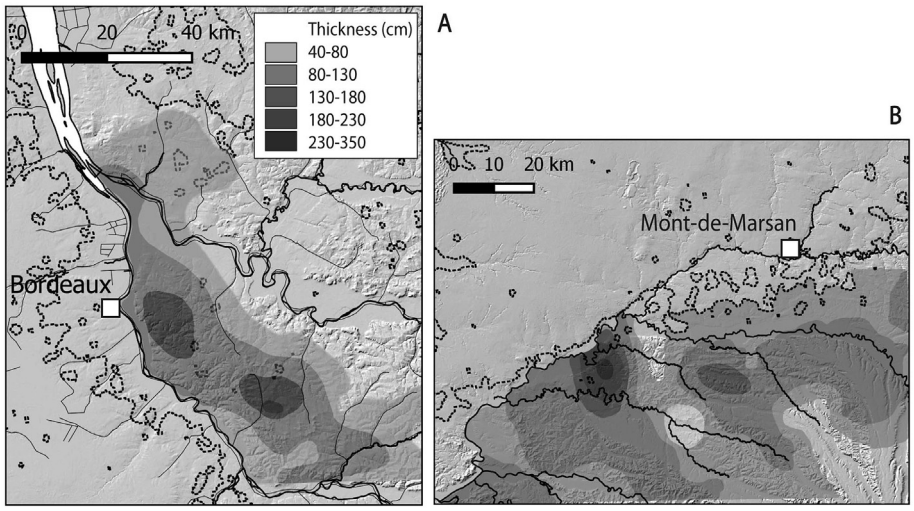

Fig. 12. Map of the thickness of the loess located on the right bank of the Garonne river (A) and on the left bank of the Adour river (B). The coversand limit is indicated by a dashed line.

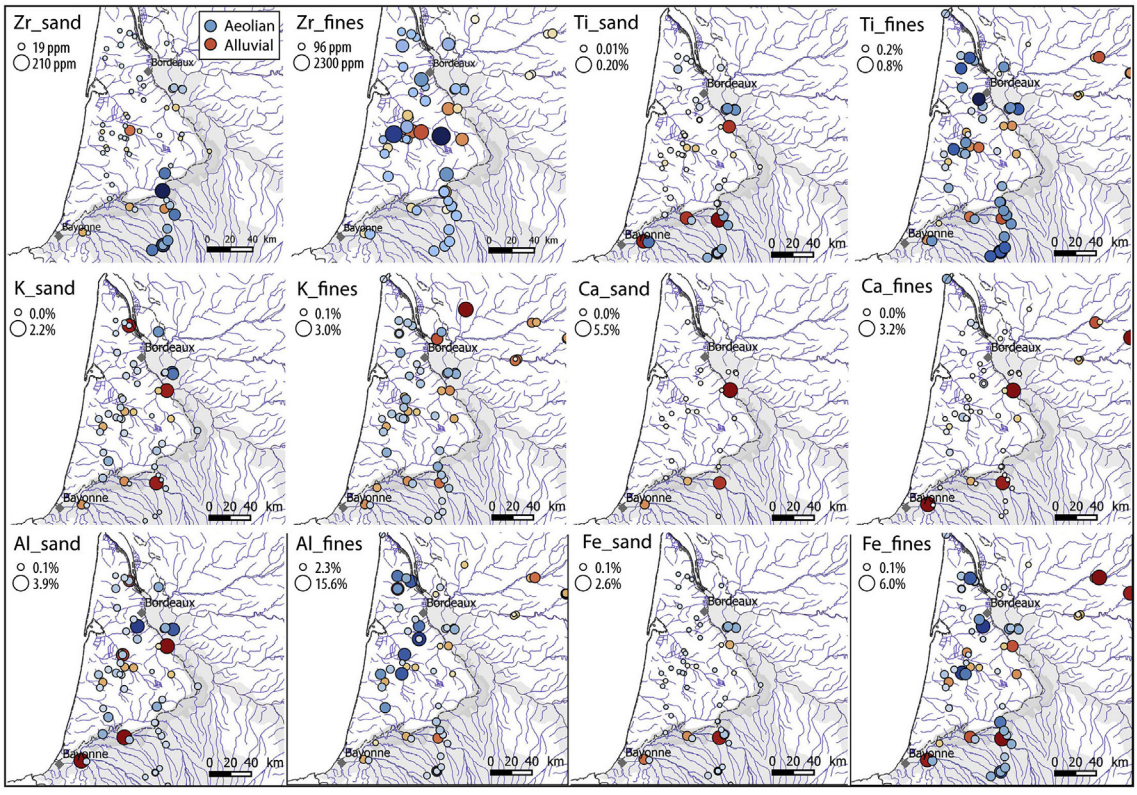

Fig. 13. Maps of the content in some elements of the aeolian and alluvial deposits. Fines = silt + clay.

thicker. For each of the LGM and MIS 3 simulations separately, the blue curve can be seen as representing the parts of the domain with scarce vegetation (mainly the coversands) and the green one, the more vegetated ones – mainly the loess areas, where part of the dust was trapped.

As a general evolution, the snow-free fraction of the surface and the depth of dry topsoil are low in the cold season and high in the warm one (Fig. 17E and F), the important question being to determine the interval when both variables are high enough to allow significant dust emissions.

In both simulations, most of the Landes surface is snow-free all year long. From October to February the depth of dry topsoil averaged over the domain is too small to allow a significant dust activity (a 5 mm threshold value was used in Sima et al., 2009, considering that the soil must be dry on at least a few mm depth for a significant dust event to occur). The dusty season could thus start in the beginning of March. At least for the LGM this is questionable, due to a warm winter bias causing an underestimation of both snow cover and soil moisture. Indeed, as mentioned in Banks et al. (2009), the simulated LGM climate over Western Europe is in

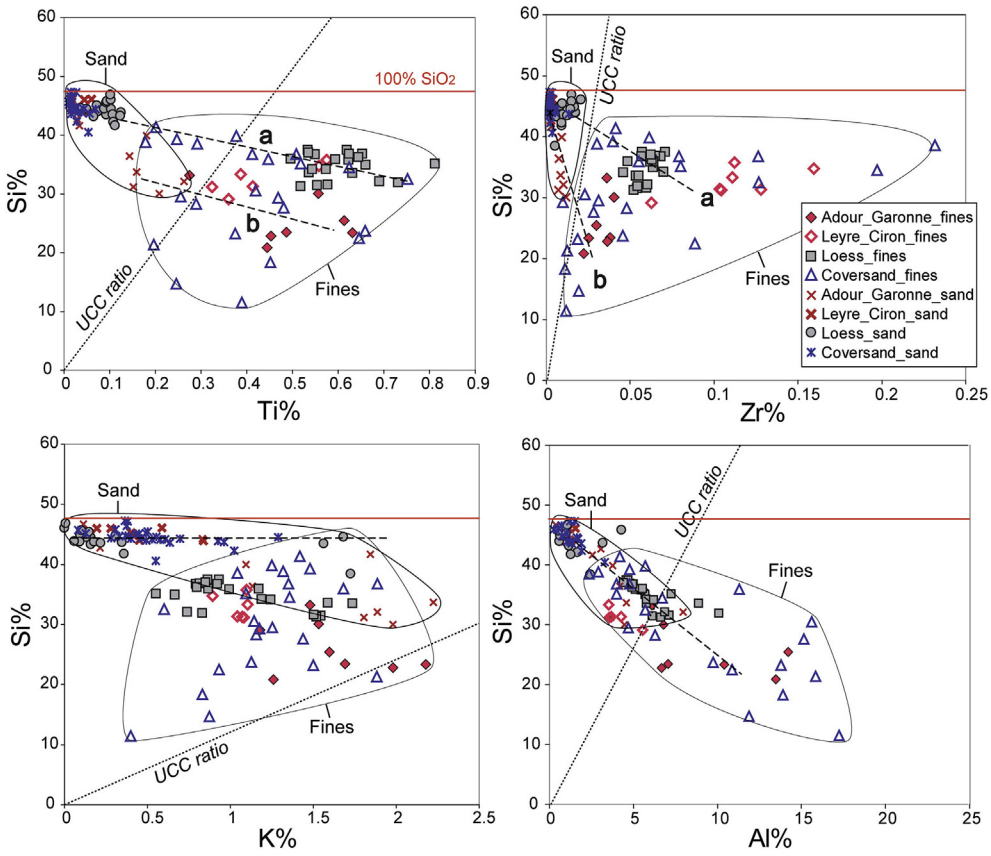

Fig. 14. Ti, Zr, K and Al – Si scattergrams of aeolian and alluvial samples of the Aquitaine basin. UCC: upper continental crust composition according to Taylor and McLennan (1995). a – adjustment line for loess and the alluvial deposits of the Leyre and Ciron rivers; b – adjustment line for other alluvial deposits.

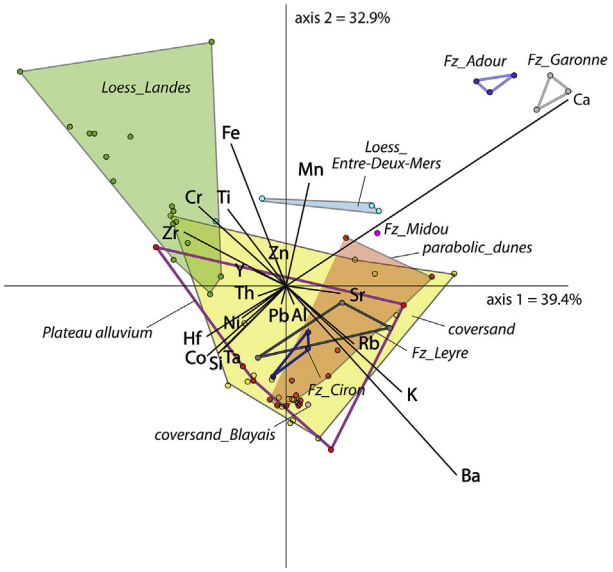

Fig. 15. Principal component analysis adapted to compositional data ("compositional biplot") of major and minor elements (fraction > 63 μm) of aeolian and potential source deposits.

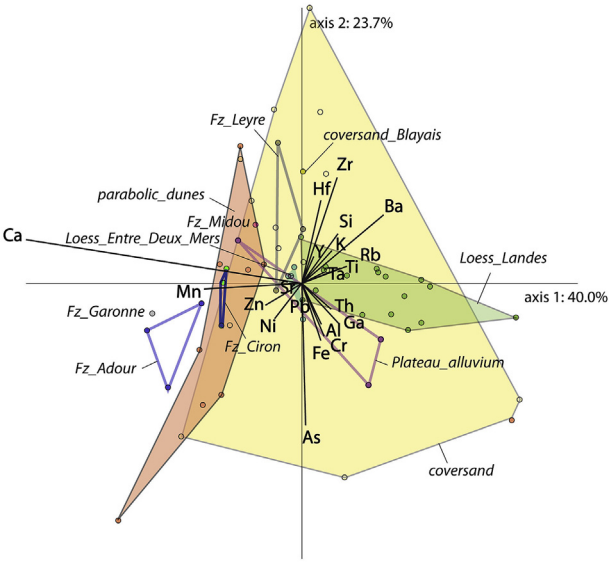

Fig. 16. Compositional biplot of major and minor elements (fraction < 63 μm) of aeolian and potential sources deposits.

agreement with pollen-based reconstructions (Wu et al., 2007) for summer and annual mean temperatures, and for mean annual precipitation, but winter cooling is underestimated by a few degrees. Thus, a comparison with the reconstructed directions for dust-efficient winds is needed to better constrain the beginning of the dusty season. Dust activity is strong until May or June, decreases to a minimum in July–August (it can even stop in more vegetated parts of the domain), and may briefly intensify again in September–October before ceasing from November to February

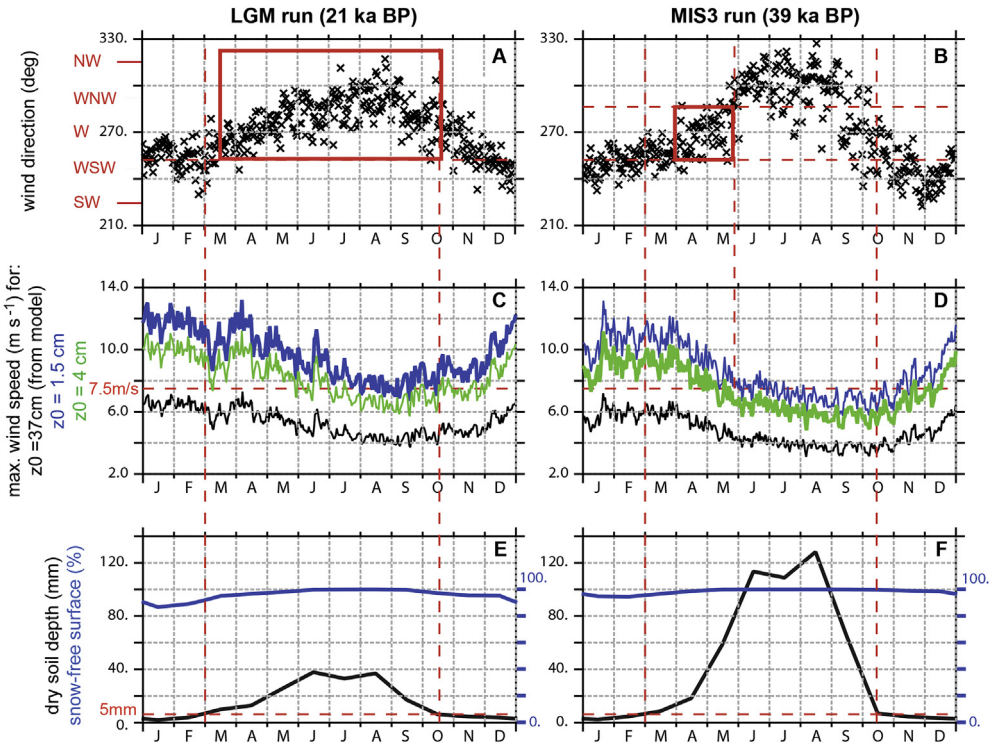

Fig. 17. Annual cycle of surface winds and ground conditions for the LGM and MIS 3 simulations (averaged over the domain between longitude 2°W-1°E and latitude 43°-45.5°N, and over 20 years for each run). From top to bottom: wind direction, daily maximum wind speed for different values of roughness length (z0), and ground conditions (dry soil depth and percent of snow-free surface). In panels (c) and (d), the thick curves (blue for LGM and green for MIS3) are the ones considered the most representative. Red dashed lines mark the different thresholds discussed in the text. Red rectangles indicate the most probable period of deflation according to the available constraints. (For interpretation of the references to colour in this figure legend, the reader is referred to the web version of this article.)

due to unfavourable surface conditions (here soil moisture, in reality probably also snow).

In the MIS 3 simulation, the average dry soil depth becomes high enough to allow significant dust emissions in the beginning of March. Dust activity stops in May due to wind weakening, which actually may be accentuated by the seasonal development of vegetation, not captured in the simulation. According to the model, in areas with scarce vegetation, dust emissions might continue to happen in the beginning of summer. Local and brief events remain possible in the rest of the summer as well, if the soil is dry, knowing that extreme wind speed values can considerably exceed the average (as also discussed above for the LGM and MIS3 winter winds). The simulated winds start to intensify again in autumn, but the increasing soil moisture plays against a restart of the emissions.

6. Discussion

6.1. Dunes

6.1.1. Low amplitude ridges

The ridges observed in the Gironde district, regardless of their morphology (transverse, barchanoid), are interpreted as zibars based on their low amplitude and the lack of slipface (Holm, 1960; Warren, 1972; Tsoar, 1978; Kocurek and Nielson, 1986; Nielson and Kocurek, 1986; Mountney and Russell, 2004). Zibars are often composed of coarse sand and the grain size is thought to be the main factor involved in preventing the development of a slipface (Bagnold, 1941; Cooke and Warren, 1973; Nielson and Kocurek, 1986).

The interpretation of the transverse and barchanoid ridges in the study area as zibars seems to be the most likely, even if they do not meet all the criteria mentioned above. Indeed, the zibars of the study area do not show a mode in coarse sands but in medium sands, similar to that found in parabolic dunes. With regards to dune morphology, we did not find in the literature zibar examples with a similar range of pattern (transverse, barchanoid, isolated ridges). Transverse and barchanoid ridges reflect unidirectional winds and point to sand transport perpendicular to the wind (Pye and Tsoar, 2009), in an environment almost devoid of vegetation.

The interpretation of the variations in dune pattern across the coversands is not straightforward, since the chronological data indicate that the ridge fields developed at different times: the barchanoid and transverse ridges in the Barp-Cestas area formed during MIS 4–3, whereas further north the barchanoid ridges date back to the Middle Pleistocene (Sitzia et al., 2015). Therefore, it remains unclear whether the morphological differences reflect changes in aeolian dynamics (especially in the availability of sand) during the same depositional phase or whether they testify to different periods of aeolian deposition. Nonetheless, it appears that topography, and particularly the slope gradient of the surface on which the ridges progressed, largely controlled their morphology.

6.1.2. Parabolic dunes

Parabolic dunes form in partially vegetated landscapes mainly under unidirectional winds, and are observed in all latitudes (Lancaster, 1995; Pye and Tsoar, 2009), along sandy coasts (Pye, 1982), but also inland (Sun and Muhs, 2007). They develop mainly from blowouts (Pye and Tsoar, 2009; Hesp, 2002; Barchyn and Hugenholtz, 2013). The morphology of parabolic dunes is controlled by the wind strength and direction, the sand supply and the nature of vegetated ground (Pye, 1982; Pye and Tsoar, 2009; Wolfe et al., 2008). The parabolic dunes gradually evolve into

elongated forms. In some cases, the arms give rise to linear dunes when the sand supply is low.

According to available OSL and ^{14}C ages (Sitzia et al., 2015), the formation of the parabolic dunes in the Landes area took place mainly during the YD. The clusters of dunes along the valleys may suggest that the sand was partly supplied by the alluvium. However, the presence of dune corridors expanding over the plateau and of dunes located on the windward side of the valleys oriented N-S (e.g. Leyre, Ciron and Avance), testifies unambiguously that the local fluvial deposits were not the main sand sources. A coastal origin for the sand transported along the corridors parallel to the wind direction appears to be the most likely.

The development of dunes along the rivers resulted from the deceleration of the winds crossing the valleys. Wiggs et al. (2002) proposed the following conceptual model: (1) on the plateau area above the valley, erosion prevails and sediment accumulation is patchy; (2) on the windward side of the valley, the wind loses its carrying capacity and sediment tends to accumulate; (3) on the opposite side of the valley, the wind accelerates and the erosive potential increases; (4) on the plateau, the wind decelerates again over a short distance promoting sand deposition. This model correctly explains the dune distribution in the study area.

6.2. Loess sources and transport dynamics

The interpolated maps of sand and silt contents suggest a genetic relationship between the aeolian facies, as previously proposed by Bertran et al. (2011, 2016). The distribution of the contour lines shows a mean NW-SE gradient at the basin scale.

In the Landes and the Blayais areas, a gradual transition between coarse and fine sand deposits can be observed, which is not controlled by the nature of the substrate but reflects wind sorting and/or decreasing carrying capacity as suggested by the distribution of current mean wind speeds (Fig. 2). The sand-silt transition is mainly controlled by the topographic change that occurs between the plateau areas (Plateau Girondin, Plateau Landais, Blayais) and the main valleys (Garonne, Adour and Dordogne). Several authors have already outlined the role played by topography in the coversand-loess transition, among others Kasse (1997), Appelman (1956) and Mason et al. (1999). In the southern part of the basin, the transitional facies (silty sands and sandy silts) form a strip on the right bank of the Adour river, showing that deposition of the suspended particles was primarily triggered by the expansion of airflows above the valley. In the northern part of the basin, the transitional facies form a narrower belt on the left (windward) side of the Garonne valley (Fig. 8), in a context broadly comparable to the Adour area. In the estuary area to the north, the maps show an almost lack of fine-grained accumulation on both sides of the valley. The sand-loess transition shifts by approximately 40 km to the east. The abundant ventifacts found on the alluvial terraces point to a deflation-dominated area.

The geochemical analysis also strongly suggests a genetic relationship between coversand and loess. The sand fraction of the southern loess is depleted in K-silicates in comparison with the coversands and correlatively enriched in quartz and resistant minerals. The enrichment is especially obvious for Zr and Ti, which concentrate mainly in the fine fraction and tend broadly to increase as a function of the distance to the coversands. Such a preferential accumulation of Zr and Ti in loess deposits has been observed worldwide (Gallet et al., 1998; Scheib et al., 2014) and is interpreted as resulting mainly from grain-size sorting. The recent alluvial deposits of the Adour river, which are rich in Ca-minerals, did not contribute significantly to dust production, which derive mainly from the coversands. In the Entre-Deux-Mers area, the alluvium of the Garonne river provided higher amounts of dust, as suggested by the larger content of easily alterable minerals in the sand fraction of the loess and, to a lesser extent, in the fine fraction. Overall, loess appears to be much more homogeneous than coversand, whose composition is closer to the alluvial sources. We assume that this homogeneity results from the mixing in the atmosphere of the different dust sources (Gallet et al., 1998).

The maps of the thickness of aeolian deposits, which cumulate several sedimentary phases, provide complementary information. In the northern part of the basin, the thickest loess deposits are located close to the Garonne valley in the Entre-Deux-Mers area and show rapid thinning toward the east (Fig. 12A). In the southern area (Fig. 12B), the loess deposits are mainly located on the left bank of the Adour river and decrease in thickness more gradually toward both the south and the east. Distinct areas of thick loess accumulation are visible on the maps but can be, at least in part, an artefact due to kriging using a limited number of data. The observed pattern of loess thickness can be explained by the following factors:

(1) The distance to the dust sources. Close to the sources, the decrease in thickness of the deposits is initially very rapid because the coarser particles, which occupy a large volume, accumulate at short distances. Farther, the decrease is more gradual and due to lower concentration of suspended particles in the dust clouds (Simonson and Hutton, 1954; Waggoner and Bingham, 1961; Frazee et al., 1970). The observed pattern points clearly to the Sable des Landes Formation and the Blayais sands as the main sources of dust. The rivers (Dordogne, Lot) flowing from the Massif Central mountains did not provide significant amounts of dust, as suggested by the lack of variation in loess thickness around the valleys. A plausible explanation is that armouring developed quickly in the dominantly coarse-grained alluvial deposits during the Glacial, preventing significant dust entrainment by deflation.

(2) A change of surface roughness related to the vegetation cover (Tsoar and Pye, 1987). It is likely that the transition between coversand and loess was associated with an increase in plant cover, which is favourable for trapping the particles. The development of vegetation is typically hampered in coversands during the phases of accumulation because of sand blasting of the young plants and of the poor water retention capacity of the superficial layer.

6.3. Pattern of dust production and accumulation

The geochemical analysis shows that northern and southern loess differ substantially in origin. For the latter, dust derived mainly from aeolian abrasion of the coversands (cf. Wright et al., 1998; Crouvi et al., 2010). Disconnection of the Landes plateau from the main drainage axes since at least the early Middle Pleistocene (Sitzia et al., 2015) due to tectonics resulted in intense redistribution of older alluvial sands by deflation and in the development of widespread coversands during the successive glacial periods. Repeated remobilization of the same aeolian sand stock together with fresh inputs from the continental shelf led to progressive enrichment of the sand material in minerals resistant to alteration (Legigan, 1979). The particle transport was predominantly NW-SE and the contribution of the alluvial plains, mainly oriented perpendicular to the wind, was low. The sand-loess transition is controlled by topography and coincides with the Adour valley (or the valleys of the tributaries).

In the northern part of the basin, dust came from aeolian abrasion of the coversands in the Blayais and the Plateau Girondin areas, and by deflation of alluvial material from the Garonne river.

Channelling of the winds by the wide Garonne corridor and higher wind speeds favoured large dust production from the plain. Dust accumulated in the Entre-Deux-Mers area to form thick deposits mostly restricted to a narrow band on the valley side.

The loess thickness, which reaches at best 3.5 m in the south and 5 m in the Entre-Deux-Mers area, is low in comparison with values observed in other European regions (Lautridou, 1985; Haase et al., 2007). Several factors have been proposed to explain the low rate of accumulation (Bertran et al., 2011): (1) a limited production of dust by aeolian abrasion of the coversands; (2) a narrow and steep continental shelf that does not allow storage of large amounts of fine alluvial sediment in the Garonne valley during sea lowstands; (3) a high soil moisture and, therefore, a low ground susceptibility to wind erosion due to an oceanic climate. The palaeoclimatic simulations both for LGM and MIS 3 agree to show that the average rainfall was significantly higher near the Atlantic coast than in Eastern Europe (Laîné et al., 2009; Kjellström et al., 2010; Strandberg et al., 2011; Sima et al., 2013) where much thicker loess deposits accumulated. However, this role remains questionable insofar as the reconstructed maximum in rainfall occurred in the winter season, which did not necessarily correspond to the most favourable period of aeolian transport.

6.4. Last-glacial wind regime from data and model constraints

The grain-size gradient together with the orientation of low-amplitude ridges and parabolic dunes allow reconstructing the prevailing wind directions of aeolian transport during the Last Glacial and the Lateglacial (Fig. 17A). The transverse ridges of the Plateau Girondin area dated to MIS 4–3 indicate efficient winds from the W. Some variability exists but appears to result from local topographical factors and from channelling of the air masses along the Garonne corridor. Unfortunately, the almost lack of MIS 2 ridge fields visible in aerial photographs does not allow getting data for this period. The crests of the MIS 2 ridges illustrated in Fig. 4 are oriented W-E, and indicate local efficient winds blowing from the north. At the basin scale the contour lines of the grain size point to winds originating from the W or the NW, and are assumed to reflect the mean direction of efficient winds during the glacial. Finally, the parabolic dunes attest for winds coming from the W-SW during the YD. The following considerations must be taken into account with regard to the reconstruction of wind directions:

(1) The accuracy of the geological proxies used may vary. The dunes are considered as the best marker for the reconstruction of past wind circulation patterns (Lancaster, 1990), especially when dunes formed under unidirectional winds (Marrs and Kolm, 1982). With regard to grain-size gradients, Renssen et al. (2007) suggested that a significant uncertainty is associated with this type of feature. The analysis made here across the Aquitaine basin, however, shows a good consistency in the regional distribution of the contour lines.
(2) The reconstructed directions of aeolian transport are indicative of the wind regimes at the regional scale during the periods of accumulation. In most of the modern sand seas, the axis of unidirectional dunes is oriented perpendicular (e.g. barchan, transverse ridges, parabolic dunes) to the dominant wind direction, i.e. the direction with the highest transport rate of sand (Fryberger and Dean, 1979). Seasonal fluctuations in wind strength are assumed to be the main factor involved in modulating the intensity of deflation. In periglacial environments, however, wind intensity is not the only factor that controls the season of aeolian transport. Other factors, particularly the snow cover and soil moisture, play a significant role on the susceptibility of the ground to deflation (Koster, 1988; Seppälä, 2004). Depending on the temperature and precipitation regimes (also determining the vegetation), different situations exist. In cold and arid environments, based on observations in the Søndre Strømfjord region (West Greenland), Dijkmans and Törnqvist (1991) have shown that aeolian transport occurred mainly during part of the winter season, whereas summer was less favourable to deflation because of vegetation growth and ground-ice melting. Based on laboratory experiments, McKenna Neuman (1989) also showed that the release of sand material susceptible to be transported by the wind can very active when the temperature drops below −20 °C because of ice sublimation. On the contrary, between −5 and −15 °C, the erosion threshold increases considerably due to the presence of a significant amount of liquid water in the ground. Dijkmans and Koster (1990), for Alaska, underline that when the snow cover is thick, the season of aeolian transport shifts towards the end of winter. According to Seppälä (2004), in arctic and subarctic regions where snow is abundant, deflation is effective only during summer, i.e. after snowmelt.

In the following, we compare our proxy data and palaeoclimatic simulations in an attempt to specify the periods of the year when dust activity occurred during the investigated climate intervals. The result depends on how reliable the simulated variables, especially the wind directions, are. In the region studied here, the atmospheric circulation is largely determined by the surface conditions (temperatures, sea-ice extent) in the North Atlantic; in glacial times, another key factor was the size of the Laurentide ice sheet (e.g., Löfverström et al., 2014; Beghin et al., 2015). In our simulation for 21 ka, these elements are imposed from reconstructions for the LGM (GLAMAP, ICE-5G). Even though these reconstructions have their uncertainties, we tend to be confident in the general aspect of the modelled annual cycle of wind directions. For the 39 ka simulation, the sea-level drop is realistic and the ice-sheet configuration is adapted to this sea-level drop, the main uncertainty being related to the North-Atlantic surface conditions. Results of numerical experiments with the LOVECLIM earth system model of intermediate complexity (van Meerbeeck et al., 2009) show a difference of air temperature of 3 °C on average over the North Atlantic between an average MIS 3 stadial state and the LGM. For the MIS 3 run examined here, the difference is 2.5 °C, close enough to the Van Meerbeeck et al. value, knowing that there was no unique (or average) MIS 3 stadial climate, but many stadial episodes differing in ice-sheet size and orbital parameters.

Since we are reasonably confident in the simulated wind directions, constraints on the dusty season can be derived using the comparison between the modelled wind directions and those reconstructed from field proxies, together with the results of sensitivity experiments with lower roughness length more typical of glacial vegetation. The only other constraining element that we can use is the simulated soil moisture, keeping in mind that it is underestimated in the cold part of the year.

In the LGM simulation, soil moisture conditions allow dust activity to start in the beginning of March, while reconstructed W-NW wind directions suggest that the dusty season should not begin before mid-March, when simulated winds change from W-SW to W (Fig. 17A). Sand transport took place during the spring/summer times because of scarce vegetation, adequate wind speeds and well-drained sandy soils. According to recent investigations (Andrieux et al., 2016), permafrost, which might have impeded drainage (Kasse, 1997), was lacking or very patchy (sporadic permafrost) during the period of sand accumulation. Deflation may have been more restricted in summer in the loess area because of

the denser vegetation cover. This scenario contrasts with that proposed by Renssen et al. (2007) for more northern latitudes, which suggested winter to be the most suitable period for deflation during MIS 2. In such a permafrost context and by comparison with the modern periglacial environments investigated by Dijkmans and Koster(1990) and Dijkmans and Törnqvist (1991), deflation was thought to have been impeded during the summer because the ground was mostly wet (thaw of the active layer), vegetation was growing, and the wind speeds were lower than in the winter season. It is worth noting that the observations in modern milieus were made on aeolian systems supplied by proglacial rivers. These rivers fed by glaciers are mostly active after the spring melt. In summer, the water table rises and, as a consequence, the sediment availability to deflation is low (Mountney and Russell, 2009). Such an aeolian system was probably characteristic of the margins of the Scandinavian ice sheet (Koster, 1988), but cannot be transposed to regions far from an ice sheet such as the Aquitaine basin. In this oceanic region, the ground was wet and largely protected by a snow cover (largely underestimated in our simulation) during the passage of winter storms, but dried in summer, thus becoming more susceptible for deflation.

In the MIS 3 simulation, the soil becomes dry enough in the beginning of March, while the reconstructed westerly winds suggest that the dusty season should not begin before the end of March. Both data and model agree that the dust activity should cease in the end of May, when the simulated winds turn from W (which is the reconstructed direction) to WNW, and the maximum wind speeds, recalculated with a roughness length value more typical of steppe vegetation (green curve in Fig. 17D), become too weak. The modelled wind directions coincide again with the reconstructed (westerly) ones in autumn, but the simulated increase in soil moisture suggests that little, if any, dust activity should occur.

Wind strength, soil moisture and snow cover determine the dusty season(s) in scarcely vegetated environments, Where vegetation has strong seasonal variations, its impact is also important. The developing vegetation contributes to wind weakening through increasing roughness length, and protects the surface against erosion, The later effect cannot be estimated here due to the unrealistically high vegetation cover in the study region, but Sima et al. (2009) have found that it stopped dust activity in the warm season under MIS 3 conditions in Europe at latitudes around 50°N.

We do not have a simulation for the YD, but we note that the annual cycle of wind direction does not considerably change between present day, LGM and MIS 3. Our results for LGM and MIS 3 are in agreement with previous results shown by van Huissteden and Pollard (2003) for winter and summer wind directions. If we suppose a certain degree of similarity between the YD and the 39 ka simulation with respect to the ice-sheet configuration and the North-Atlantic surface conditions (roughly halfway between full glacial and interglacial states), we may speculate that winter, typified by dominantly W-SW wind directions, was the main period of sand transport during the YD. In Western Europe, winter is the season that corresponds to the passage of the main perturbations and associated storms, and that records the highest wind speeds (Fig. 17C and D). These wind directions are in agreement with those reconstructed for the YD by Isarin et al. (1997). The YD orientation of parabolic dunes in Aquitaine is identical to that observed in the Netherlands (Isarin et al., 1997) and should be associated with increased speed of SW winds throughout Northwestern and Western Europe (Isarin et al., 1997). Differences should have been important in the surface conditions, which for the YD allowed dust activity in winter: scarce vegetation, reduced snow cover compared to LGM and MIS 3, and reduced soil moisture favoured by improved ground drainage due to the lack of permafrost and to the weaker influence of meltwater from the ice sheets (for Northern Europe).

7. Conclusions

The multi-approach study of the aeolian deposits of southwest France allows better understanding of sediment sources and depositional dynamics. The maps of interpolated grain size and the geochemical composition converge to show a genetic relationship between coversands and finer-grained deposits. In the southern part of the basin, dust derived mainly from aeolian abrasion of the coversands and is dominantly composed of minerals resistant to alteration. In contrast, both the coversands and the floodplain of the Garonne river, richer in Ca-bearing minerals, contributed to loess in the northern part of the basin.

The low-amplitude dunes lacking slipfaces, dated to MIS 4–3, are interpreted as zibars and show variable morphologies (transverse, barchanoid, isolated barchanoid) occurring as strips subparallel to the coastline. This pattern seems to be mainly controlled by the slope gradient. The parabolic dunes dated to the YD are simple, complex or compound. These are clustered along the rivers but are rare on the plateaus, which correspond to deflation areas. In the valleys oriented W-E, i.e. parallel to the prevailing winds, corridors of elongated parabolic dunes developed, whereas more simple shapes occur on both sides of the valleys perpendicular to the winds. These formed as a consequence of relief-induced deceleration of the airflows. Overall, the dune distribution indicates that the sand supply came mainly from the coast.

The spatial analysis of dune shapes and grain-size gradients, as well as the study of dust sources, made it possible reconstructing the Last Glacial wind regimes in the study region. The efficient winds changed significantly through time. They came from the W to the NW during the glacial, and the W-SW during the YD. They were generally stronger during the LGM than during MIS3, according to the simulations used here. The comparison between proxy data and both the current and simulated Last Glacial wind regimes strongly suggests that aeolian transport of sand and dust occurred mostly during the spring/summer season for the glacial, and the winter for the YD. We assume that these variations were not related to changes in the pattern of atmospheric circulation, but rather to changes in the deflation season. This was mainly controlled by the length of the season with a snow cover and frozen or moist ground, and by the seasonal evolution of the wind speeds able to cause deflation. Vegetation could impose additional constraints in areas or periods when its seasonal variations were significant.

Acknowledgments

We acknowledge Christophe Tuffery (Inrap) for his help in the GIS. This work was funded by Inrap, the University of Bordeaux and Lascarbx (Universités de Bordeaux, program of the Agence Nationale de la Recherche ANR-10-LABX-52). The Labex L-IPSL, which is funded by the ANR (grant #ANR-10-LABX-0018), is also acknowledged. This is LDEO #8118. The two anonymous reviewers are also thanked for their remarks, which contributed to greatly improve the manuscript. The simulations used here have been run on the HPC facilities of the Commissariat à l'Energie Atomique.

Appendix A. Supplementary data

Supplementary data related to this article can be found at http://dx.doi.org/10.1016/j.quascirev.2017.06.029.

References

Aitchison, J., 1982. The statistical analysis of compositional data. J. R. Stat. Soc. Ser. B Methodol. 44, 139–177.

Aitchison, J., 1986. The Statistical Analysis of Compositional Data. Chapman & Hall, London, UK, 416 pp.

Aitchison, J., Greenacre, M., 2002. Biplots of compositional data. J. R. Stat. Soc. Ser. C Appl. Statistics) 51, 375–392.

Andrieux, E., Bertran, P., Saito, K., 2016. Spatial analysis of the French Pleistocene permafrost by a GIS database. Permafr. Periglac. Process. 27, 17–30.

Ahn, H., Park, S., Chang, L., 2007. Effect of direct radiative forcing of Asian dust on the meteorological fields in East Asia during an Asian dust event period. J. Appl. Meteorology Climatol. 46, 1655–1681.

Antoine, P., Rousseau, D.-D., Zöller, L., Lang, A., Munaut, A.-V., Hatté, C., Fontugne, M., 2001. High-resolution record of the last interglacial-glacial cycle in the nussloch loess-palaeosol sequences, upper rhine area, Germany. Quat. Int. 76–77, 211–229.

Appelman, F., 1956. Variation de la composition granulométrique des sédiments éoliens en rapport avec leur latitude et leur altitude. Pédologie VI 26–37.

Ballabio, C., Panagos, P., Monatanarella, L., 2016. Mapping topsoil physical properties at European scale using the LUCAS database. Geoderma 261, 110–123.

Bagnold, R.A., 1941. The Physics of Wind Blown Sand and Desert Dunes. Methuen, London, 265 pp.

Banks, W.E., Zilhão, J., d'Errico, F., Kageyama, M., Sima, A., Ronchitelli, A., 2009. Investigating links between ecology and bifacial tool types in western Europe during the last glacial maximum. J. Archaeol. Sci. 36, 2853–2867.

Barchyn, T.E., Hugenholtz, C.H., 2013. Reactivation of supply-limited dune fields from blowouts: a conceptual framework for state characterization. Geomorphology 201, 172–182.

Beghin, P., Charbit, S., Dumas, C., Kageyama, M., Ritz, y C., 2015. How might the North American ice sheet influence the northwestern Eurasian climate? Clim. Past 11, 1467–1490.

Berger, A., 1978. Long-term variations of caloric solar radiation resulting from the earth's orbital elements. Quat. Res. 9, 139–167.

Bertran, P., Allenet, G., Gé, T., Naughton, F., Poirier, P., Goñi, M.F.S., 2009. Coversand and Pleistocene palaeosols in the Landes region, southwestern France. J. Quat. Sci. 24, 259–269.

Bertran, P., Bateman, M.D., Hernandez, M., Mercier, N., Millet, D., Sitzia, L., Tastet, J.-P., 2011. Inland aeolian deposits of south-west France: facies, stratigraphy and chronology. J. Quat. Sci. 26, 374–388.

Bertran, P., Liard, M., Sitzia, L., Tissoux, H., 2016. A map of Pleistocene aeolian deposits in Western Europe, wiht special emphasis on France. J. Quat. Sci. 31 (8), 844–856.

Braconnot, P., 2004. Modeling the last glacial maximum and mid-holocene. Comptes Rendus Geosci. 336, 711–719.

Buurman, P., Pape, T., Reijneveld, J.A., de Jong, F., van Gelder, E., 2001. Laser-diffraction and pipette-method grain sizing of Dutch sediments: correlations for fine fractions of marine, fluvial, and loess samples. Neth. J. Geosciences 80, 49–57.

Capdeville, J.-P., Dubreuilh, J., 1994. Les formations superficielles du Bassin d'Aquitaine: identification, potentialités, contraintes. BRGM report R-38 271, Orléans, 52 pp.

Comas-Cufí, M., Thió-Henestrosa, S., 2011. CoDaPack 2.0: a Stand-alone, Multi-platform Compositional Software. http://ima.udg.edu/codapack/ (Accessed 06 July 2016).

Cooke, R.U., Warren, A., 1973. Geomorphology in Deserts. University of California Press, 448 pp.

Crouvi, O., Amit, R., Enzel, Y., Gillespie, A.R., 2010. Active sand seas and the formation of desert loess. Quat. Sci. Rev. 29, 2087–2098.

De Vos, W., Tarvainen, T., Salminen, R., Reeder, S., De Vivo, B., Demetriades, A., Pirc, S., Batista, M.J., Marsina, K., Ottesen, R.T., O'Connor, P.J., Bidovec, M., Lima, A., Siewers, U., Smith, B., Taylor, H., Shaw, R., Salpeteur, I., Gregorauskiene, V., Halamic, J., Slaninka, I., Lax, K., Gravesen, P., Birke, M., Breward, N., Ander, E.L., Jordan, G., Duris, M., Klein, P., Locutura, J., Bel-lan, A., Pasieczna, A., Lis, J., Mazreku, A., Gilucis, A., Heitzmann, P., Klaver, G., Petersell, V., 2006. Geochemical Atlas of Europe. Part 2-Interpretation of Geochemical Maps, Additional Tables, Figures, Maps, and Related Publications. Geological Survey of Finland, Espoo.

Dijkmans, J.W.A., Koster, E.A., 1990. Morphological development of dunes in a subarctic environment, central Kobuk valley, northwestern Alaska. Geografiska Annaler. Ser. A, Phys. Geogr. 72, 93–109.

Dijkmans, J.W.A., Törnqvist, T.E., 1991. Modern periglacial eolian deposits and landforms in the Søndre Strømfjord area, West Greenland and their palaeoenvironmental implications. Meddelelser om Grønland. Geoscience 25, 3–39.

Dubreuilh, J., 1976. Contribution à l'étude sédimentologique du système fluviatile Dordogne-Garonne dans la région bordelaise. Thèse d'état. Université de Bordeaux, Bordeaux, 273 pp.

Dubreuilh, J., Capdeville, J.P., Farjanel, G., Karnay, G., Platel, J.P., Simon-Coinçon, R., 1995. Dynamique d'un comblement continental néogène et quaternaire: l'exemple du bassin d'Aquitaine. Géologie la Fr. 4, 3–26.

Duchaufour, P., 1997. Abrégé de pédologie : sol, végétation, environnement. Masson, Paris, 285 pp.

Enjalbert, H., 1960. Les Pays Aquitains : Le modelé et les sols. Imprimerie Bière, Bordeaux.

Egozcue, J., Pawlowsky-Glahn, V., Mateu-Figueras, G., Barcelo - Vidal, C., 2003. Isometric logratio transformations for compositional data analysis. Math. Geol. 35 (3), 279–300.

Ewing, R.C., Kocurek, G., Lake, L.W., 2006. Pattern analysis of dune-field parameters. Earth Surf. Process. Landforms 31, 1176–1191.

Fralick, B.W., Kronberg, B.I., 1997. Geochemical discrimination of clastic sedimentary rock sources. Sediment. Geol. 113, 111–124.

Frazee, C.J., Fehrenbacher, J.B., Krumbein, W.C., 1970. Loess distribution from a source. Soil Sci. Soc. Am. J. 34, 296–301.

Fryberger, S.G., Dean, G., 1979. Dune forms and wind regime. In: McKee, E.D. (Ed.), A Study of Global Sand Seas, Geological Survey Professional Paper 1052. United States Government Printing Office, Washington DC, pp. 137–171.

Gallet, S., Jahn, B., Van Vliet Lanoë, B., Dia, A., Rossello, E., 1998. Loess geochemistry and its implications for particle origin and composition of the upper continental crust. Earth Planet. Sci. Lett. 156, 157–172.

Haase, D., Fink, J., Haase, G., Ruske, R., Pécsi, M., Richter, H., Altermann, M., Jäger, K.-D., 2007. Loess in Europe—its spatial distribution based on a European loess map, scale 1:2.500.000. Quat. Sci. Rev. 26, 1301–1312.

Hernandez, M., Mercier, N., Bertran, P., Colonge, D., Lelouvier, L.A., 2012. Premiers éléments de datation des industries du Pléistocène moyen (Acheuléen - paléolithique moyen ancien) de la région pyrénéo-garonnaise : une approche géochronologique pluri-méthodes (TL, OSL et TT-OSL) des sites de Duclos et Romentères. Paléo 23, 155–170.

Hesp, P., 2002. Foredunes and blowouts: initiation, geomorphology and dynamics. Geomorphology 48, 245–268.

Holm, D.A., 1960. Desert geomorphology in the Arabian peninsula. Science 132, 1369–1379.

INRA, 2011. Donesol Version 2.0.5. http://acklins.orleans.inra.fr/outil/donesol/dictionnaire_donesol_igcs_2011-02-25.pdf (Accessed 05 July 2016).

Isarin, R.F.B., Renssen, H., Koster, E.A., 1997. Surface wind climate during the Younger Dryas in Europe as inferred from aeolian records and model simulations. Palaeogeogr. Palaeoclimatol. Palaeoecol. 134, 127–148.

ISO, 2009. ISO 13320, Particle Size Analysis -Laser Diffraction Methods.

Jones, R.M., 2003. Particle Size Analysis by Laser Diffraction: ISO 13320, Standard Operating Procedures, and Mie Theory. American Laboratory.

Karnay, G., Corbier, P., Bourgine, B., Saltel, M., 2010. Gestion des eaux souterraines en région Aquitaine. Reconnaissance des potentialités aquifères du Mio-Plio-Quaternaire des Landes de Gascogne et du Médoc en relation avec les SAGE. BRGM report RP 57813, Orléans, 73 pp.

Kasse, C., 1997. Cold-climate aeolian sand-sheet formation in North-Western Europe (c. 14–12.4 ka); a response to permafrost degradation and increased Aridity. Permafr. Periglac. Process. 8, 295–311.

Kjellström, E., Brandefelt, J., Näslund, J.-O., Smith, B., Strandberg, G., Voelker, A.H.L., Wohlfarth, B., 2010. Simulated climate conditions in Europe during the marine isotope stage 3 stadial. Boreas 39, 436–456.

Klingebiel, A., 1966. Observations sur les sables de recouvrement superficiel dans le bordelais. Bull. la carte géologique la Fr. t. LXI 278, 185–188.

Kocurek, G., Nielson, J., 1986. Conditions favourable for the formation of warm-climate aeolian sand sheets. Sedimentology 33, 795–816.

Konert, M., Vandenberghe, J., 1997. Comparison of laser grain size analysis with pipette and sieve analysis: a solution for the underestimation of the clay fraction. Sedimentology 44, 523–535.

Koster, E.A., 1988. Ancient and modern cold-climate aeolian sand deposition: a review. J. Quat. Sci. 3, 69–83.

Krinner, G., Viovy, N., de Noblet-Ducoudré, N., Ogée, J., Polcher, J., Friedlingstein, P., Ciais, P., Sitch, S., Prentice, I.C., 2005. A dynamic global vegetation model for studies of the coupled atmosphere-biosphere system. Glob. Biogeochem. Cycles 19, GB1015.

Laîné, A., Kageyama, M., Salas-Mélia, D., Valdoire, A., Rivière, G., Ramstein, G., Planton, S., Tyteca, S., Peterschmidtt, J.Y., 2009. Northern Hemisphere storm tracks during the last glacial maximum in the PMIP2 ocean-atmosphere coupled models: energy study, seasonal cycle, precipitation. Clim. Dyn. 32, 593–614.

Lancaster, N., 1995. In: Richards, K. (Ed.), Geomorphology of Desert Dunes. Routledge Physical Environment Series. Routledge, London, New York, 290 pp.

Lancaster, N., 1990. Palaeoclimatic evidence from sand seas. Palaeogeogr. Palaeoclimatol. Palaeoecol. 76, 279–290.

Lautridou, J.-P., 1985. Le cycle périglaciaire pleistocène en Europe du nord-ouest et plus particulièrement en Normandie. Thèse d'état. Université de Caen, Centre de géomorphologie du C.N.R.S, Caen, France, 908 pp.

Léger, M., 1990. Loess landforms. Quat. Int. 7/8, 53–61.

Legigan, P., 1979. L'élaboration de la formation du Sable des Landes. Mémoire de l'Institut de Géologie du Bassin d'Aquitaine, Bordeaux, 429 pp.

Liu, T., 1988. Loess in China. Springer Series in Physical Environment. Springer, Berlin, 224 pp.

Löfverström, M., Caballero, R., Nilsson, J., Kleman, J., 2014. Evolution of the large-scale atmospheric circulation in response to changing ice sheets over the last glacial cycle. Clim. Past 10, 1453–1471. http://dx.doi.org/10.5194/cp-10-1453-2014.

Maarleveld, G.C., 1960. Wind directions and cover sands in The Netherlands. Biul. Peryglac. 8, 49–58.

Special paper 192,. In: Marrs, R.W., Kolm, K.E. (Eds.), 1982. Interpretation of Windflow Characteristics from eolian Landforms. Geological society of America, Boulder, USA, 109 pp.

Martín-Fernández, J., Barceló-Vidal, C., Pawlowsky-Glahn, V., 2003. Dealing with

zeros and missing values in compositional data sets using nonparametric imputation. Math. Geol. 35, 253–278.
Mason, J.A., 2001. Transport direction of peoria loess in Nebraska and implications for loess sources on the central great plains. Quat. Res. 56, 79–86.
Mason, J.A., Nater, E.A., Zanner, C.W., Bell, J.C., 1999. A new model of topographic effects on the distribution of loess. Geomorphology 28, 223–236.
McKee, E.D., 1979. Introduction to a study of global sand seas. Geological Survey Professional Paper 1052. In: McKee, E.D. (Ed.), A Study of Global Sand Seas. United States Government Printing Office, Washington DC, pp. 1–19.
McKenna Neuman, C., 1989. Kinetic energy transfer through impact and its role in entrainment by wind of particles from frozen surfaces. Sedimentology 36, 1007–1015.
Melkerud, P.A., Bain, D.C., Jongmans, A.G., Tarvainen, T., 2000. Chemical, mineralogical and morphological characterization of three podzols developed on glacial deposits in Northern Europe. Geoderma 94, 125–148.
Mountney, N.P., Russell, A.J., 2009. Aeolian dune-field development in a water table controlled system: Skeiðarársandur, Southern Iceland. Sedimentology 56, 2107–2131.
Mountney, N.P., Russell, A.J., 2004. Sedimentology of cold-climate aeolian sandsheet deposits in the Askja region of northeast Iceland. Sediment. Geol. 166, 223–244.
Muhs, D.R., Bettis, E.A., Aleinikoff, J.N., McGeehin, J.P., Beann, J., Skipp, G., Marshall, B.D., Roberts, H.M., Johnson, W.C., Benton, R., 2008. Origin and paleoclimatic significance of late Quaternary loess in Nebraska: evidence from stratigraphy, chronology, sedimentology, and geochemistry. Geol. Soc. Am. Bull. 120, 1378–1407.
Nielson, J., Kocurek, G., 1986. Climbing zibars of the Algodones. Sediment. Geol. 48, 1–15.
Pannatier, Y., 1996. Variowin: Software for Spatial Data Analysis in 2D, Statistics and Computing. Springer, New York, Berlin, London, Paris, 91 pp.
Paul, A., Schäfer-Neth, C., 2003. Modeling the water masses of the Atlantic Ocean at the last glacial maximum. Paleoceanography 18, 1058.
Pawlowsky-Glahn, V., Olea, R.A., 2004. Geostatistical Analysis of Compositional Data. Oxford University Press, Oxford, 204 pp.
Pawlowsky, V., Burger, H., 1992. Spatial structure analysis of regionalized compositions. Math. Geol. 24, 675–691.
Peltier, W.R., 2004. Global glacial isostasy and the surface of the ice-age earth: the ICE-5G (VM2). Model GRACE Annu. Rev. Earth Planet. Sci. 32, 111–149.
Poser, H., 1950. Zur Rekonstruktion der spätglazialen Luftdruckverhältnisse in Mittelund Westeuropa auf Grund der vorzeitlichen binnenDünen. Erdkunde 4, 81–88.
Pye, K., 1982. Morphological development of coastal dunes in a humid tropical environment, Cape Bedford and Cape Flattery, North Queensland. Geografiska Annaler. Ser. A, Phys. Geogr. 64, 213–227.
Pye, K., Tsoar, H., 2009. Aeolian Sand and Sand Dunes. Springer, Berlin, Heidelberg, 458 pp.
Raynaud, D., Jouzel, J., Barnola, J.M., Chapellaz, J., Delmas, R.J., Lorius, C., 1993. The ice record of greenhouse gases. Science 259, 926–934.
Reimann, C., Demetriades, A., Birke, M., Filzmoser, P., O'Connor, P., Halamić, J., Ladenberger, A., The GEMAS Project Team, 2014. Distribution of elements/parameters in agricultural and grazing land soil of Europe. In: Reimann, C., Birke, M., Demestriades, A., Filzmoser, P., O'Connor, P. (Eds.), Chemistry of Europe's Agricultural Soils, Part a: Methodology and Interpretation of the GEMAS Data Set, Geologisches Jahrbuch, Reihe B, vol. 102, pp. 103–523.
Renssen, H., Kasse, C., Vandenberghe, J., Lorenz, S.J., 2007. Weichselian Late Pleniglacial surface winds over northwest and central Europe: a model–data comparison. J. Quat. Sci. 22, 281–293.
Righi, D., De Coninck, F., 1974. Micromorphological aspects of Humods and Haplaquods of the Landes du Médoc, France. In: Rutherford, G.K. (Ed.), Soil Microscopy. Limestone Press, Kingston, Ontario, pp. 567–588.
Rousseau, D.D., Chauvel, C., Sima, A., Hatté, C., Lagroix, F., Antoine, P., Balkanski, Y., Fuchs, M., Mellett, C., Kageyama, M., Ramstein, G., Lang, A., 2014. European glacial dust deposits: geochemical constraints on atmospheric dust cycle modeling. Geophys. Res. Lett. 41, 7666–7674. http://dx.doi.org/10.1002/2014GL061382.
Ruegg, G.H.J., 1983. Periglacial eolian evenly laminated sandy deposits in the late Pleistocene of nw Europe, a facies unrecorded in modern sedimentological handbooks. In: Developments in Sedimentology. Elsevier, pp. 455–482.
Sarnthein, M., Gersonde, R., Niebler, S., Pflaumann, U., Spielhagen, R., Thiede, J., Wefer, G., Weinelt, M., 2003. Overview of glacial Atlantic Ocean mapping (GLAMAP 2000). Paleoceanography 18, 1030.
Scheib, A.J., Birke, M., Dinelli, E., GEMAS Project Team, 2014. Geochemical evidence of aeolian deposits in European soils. Boreas 43, 175–192.
Seppälä, M., 2004. Wind as a Geomorphic Agent in Cold Climates. Cambridge University press, Cambridge, 358 pp.
Sima, A., Rousseau, D.-D., Kageyama, M., Ramstein, G., Schulz, M., Balkanski, Y., Antoine, P., Dulac, F., Hatté, C., 2009. Imprint of North-Atlantic abrupt climate changes on western European loess deposits as viewed in a dust emission model. Quat. Sci. Rev. 28, 2851–2866.
Sima, A., Kageyama, M., Rousseau, D.-D., Ramstein, G., Balkanski, Y., Antoine, P., Hatté, C., 2013. Modeling dust emission response to North Atlantic millennial-scale climate variations from the perspective of East European MIS 3 loess deposits. Clim. Past 9, 1385–1402.
Simonson, R.W., Hutton, C.E., 1954. Distribution curves for loess. Am. J. Sci. 252, 99–105.
Sitzia, L., Bertran, P., Bahain, J.-J., Bateman, M.D., Hernandez, M., Garon, H., de Lafontaine, G., Mercier, N., Leroyer, C., Queffelec, A., Voinchet, P., 2015. The Quaternary coversands of southwest France. Quat. Sci. Rev. 124, 84–105.
Stevens, T., Palk, C., Carter, A., Lu, H., Clift, P.D., 2010. Assessing the provenance of loess and desert sediments in northern China using U-Pb dating and morphology of detrital zircons. Geol. Soc. Am. Bull. 122, 1331–1344.
Strandberg, G., Brandefelt, J., Kjellström, E., Smith, B., 2011. High resolution simulation of last glacial maximum climate in Europe. Tellus 63 A, 107–125.
Sun, J., Muhs, D.R., 2007. Dune fields | mid-latitudes. In: Elias, S.A. (Ed.), Encyclopedia of Quaternary Science. Elsevier, Oxford, pp. 607–626.
Taylor, S.R., McLennan, S.M., 1995. The geochemical evolution of the continental crust. Rev. Geophys. 33, 241–265.
Thibault, C., 1970. Recherches sur les terrains quaternaires du bassin de l'Adour. Thèse d'état. Université de Bordeaux, Bordeaux, 814 pp.
Tsoar, H., 1978. The Dynamics of Longitudinal Dunes (Final technical report). DTIC Document. European Research Office, US Army, 171 pp, London.
Tsoar, H., Pye, K., 1987. Dust transport and the question of desert loess formation. Sedimentology 34, 139–153.
Van Huissteden, K., Schwan, J.C.G., Bateman, M.D., 2001. Environmental conditions and paleowind directions at the end of the Weichselian Late Pleniglacial recorded in aeolian sediments and geomorphology (Twente, Eastern Netherlands). Geol. en Mijnbouw/Neth. J. Geosciences 80, 1–18.
van Huissteden, K., Pollard, D., 2003. Oxygen isotope stage 3 fluvial and eolian successions in Europe compared with climate model results. Quat. Res. 59, 223–233.
van Meerbeeck, C.J., Renssen, H., Roche, D.M., 2009. How did marine isotope stage 3 and last glacial maximum climates differ? – perspectives from equilibrium simulations. Clim. Past 5, 33–51.
Waggoner, P.E., Bingham, C., 1961. Depth of loess and distance from source. Soil Sci. 92, 396–401.
Warren, A., 1972. Observations on dunes and Bi-Modal sands in the ténéré desert. Sedimentology 19, 37–44.
Webster, R., Oliver, M.A., 2007. Geostatistics for Environmental Scientists. Statistics in Practice. Wiley, Chichester, 315 pp.
Wedepohl, K.H., 1978. Handbook of Geochemistry. Springer-Verlag, Berlin, Heidelberg, 443 pp.
Wiggs, G., Bullard, J., Garvey, B., Castro, I., 2002. Interactions between airflow and valley topography with implications for aeolian sediment transport. Phys. Geogr. 23, 366–380.
Wojdyr, M.J., 2010. Fityk: a general-purpose peak fitting program. J. Appl. Crystallogr. 43, 1126–1128.
Wolfe, S.A., Moorman, B.J., Hugenholtz, C.H., 2008. Effects of sand supply on the morphodynamics and stratigraphy of active parabolic dunes, Bigstick Sand Hills, southwestern Saskatchewan. Can. J. Earth Sci. 45, 321–335.
Wright, J., Smith, B., Whalley, B., 1998. Mechanisms of loess-sized quartz silt production and their relative effectiveness: laboratory simulations. Geomorphology 23, 15–34.
Wu, H., Guiot, J., Brewer, S., Guo, Z., 2007. Climatic changes in Eurasia and Africa at the last glacial maximum and mid-Holocene: reconstruction from pollen data using inverse vegetation modelling. Clim. Dyn. 29, 211–229.
Zeeberg, J., 1998. The European sand belt in Eastern Europe - and comparison of Late Glacial dune orientation with GCM simulation results. Boreas 27, 127–139.

Last glacial wind regime in southwest France derived from dunes, grain-size gradients and loess geochemistry.

Luca Sitzia, Pascal Bertran, Adriana Sima, Philippe Chery, Alain Queffelec, Denis-Didier Rousseau

Supplementary data

1. Grain-size analysis

The pre-treatment of samples for particle-size analysis included i) suspension in sodium hexametaphosphate (5 g/L) and hydrogen peroxide (35%) during 12 hours, and ii) 60 seconds of ultrasonification in the microgranulometer to achieve optimal dispersion. We used a HORIBA LA950 (0.01µm - 3000µm) laser microgranulometer and analysed the data with the NextSpec 7.10 software. The Mie solution to Maxwell's equations (also called Lorenz-Mie or Lorenz-Mie-Debye solution, Hergert and Wriedt, 2012) provided the basis for calculating the particle size (Mie, 1908) as is recommended by the ISO committee (Jones, 2003; ISO, 2009). We applied this solution to calculate the particle-size distribution in aqueous solution (refractive index 1,333) and chose a refractive index for the particles of 1.55i - 0.01i. This value gave the best fit between the measured diffracted light pattern and the iteratively-calculated one as indicated by the R parameter (eq. 1) (Bullimer, 2013).

$$R = \frac{1}{N}\sum_{i=1}^{N}\left\{\frac{1}{y(x_i)}\left|y_i - y(x_i)\right|\right\} \qquad (1)$$

N = The number of detectors used for the calculation
y_i = The measured scattered light at each channel (i) of the detector
$y(x_i)$ = The calculated scattered light at each channel (i) of the detector based on the chosen refractive index kernel and the reported particle-size distribution.

The Fraunhofer approximation to Maxwell's equation, despite its general use in particle-size analysis, is far from allowing such a good fit (de Boer et al., 1987; Bullimer, 2013). To demonstrate the impact of the choice of the algorithm in particle-size analysis by laser diffraction, we calculated the size distribution for some representative samples by using different algorithms and refractive indices on the same measurement made by the microgranulometer. The ternary plot (fig. SI_1) shows how different can be the compositions obtained. As shown by the sample "Pot-aux-Pins", which is mostly sand, the Fraunhofer approximation is correct for large particles and the particle-size distributions of sandy samples are similar whatever the algorithm used. In contrast, finer-grained samples give strongly scattered results. Figure SI_3 and Table SI_1 point to a poor fit (high R value) of the calculated signal with the measured one for the high angles of diffraction (i.e. for fine-grained particles) using the Fraunhofer algorithm. For the Mie algorithm, the particle size distribution (Fig. SI_2) is also strongly influenced by the refractive index chosen. The number and size of the modes, and the proportion of the different size classes vary significantly according to the refractive index (Table SI_1).

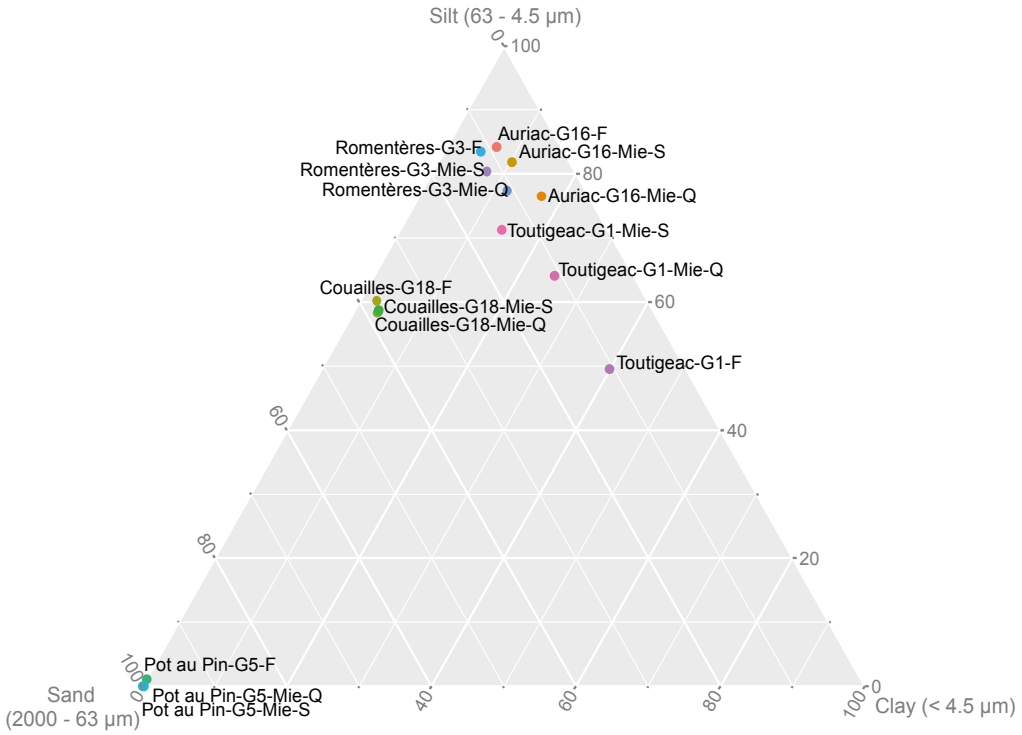

Figure SI_1: Ternary diagram where the particle-size distributions calculated with the different algorithms and refractive indices are plotted. F: Fraunhofer, Mie-Q: Mie with the refractive index of quartz (1.45 - 0.00i), Mie-S: Mie with the refractive index of sediment (1.55 - 0.01i).

Sample-Algorithm	R	D10 (µm)	D50 (µm)	D90 (µm)	% Sand (2000-63 µm)	% Silt (63-4,5 µm)	% Clay (<4.5µ)
Auriac-G16-F	0,1292	5,2937	14,4613	59,0022	8,8659	84,2154	6,92
Auriac-G16-Mie-Q	0,072214	2,8817	20,5694	52,032	6,5025	76,5372	16,96
Auriac-G16-Mie-S	0,035178	4,4275	16,7085	55,7339	7,9268	81,863	10,21
Toutigeac-G1-F	0,17948	1,5858	8,3543	65,3287	10,5859	49,5153	39,9
Toutigeac-G1-Mie-Q	0,071635	1,0649	20,4792	66,832	10,9141	64,1188	24,97
Toutigeac-G1-Mie-S	0,059117	3,3708	16,968	87,2931	14,6276	71,264	14,11

Table SI_1: R parameter and sedimentological values for calculations using the different algorithms for two samples (Auriac-G16 and Toutigeac-G1).

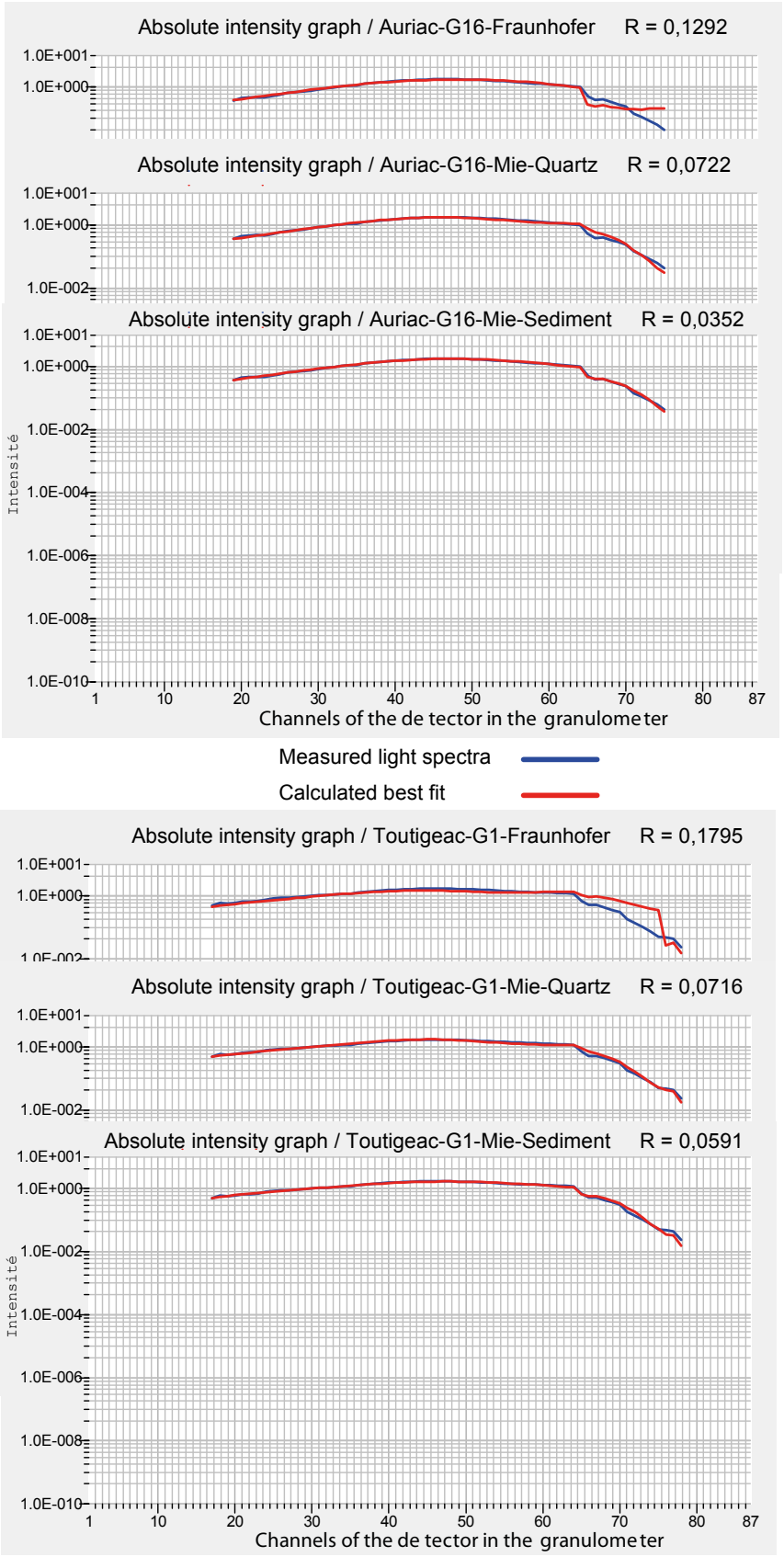

Figure SI_2: Comparison of calculated vs. measured diagrams using different algorithms and refractive indices. The high numbered channels correspond to high angles of diffracted light mostly due to diffraction by small particles.

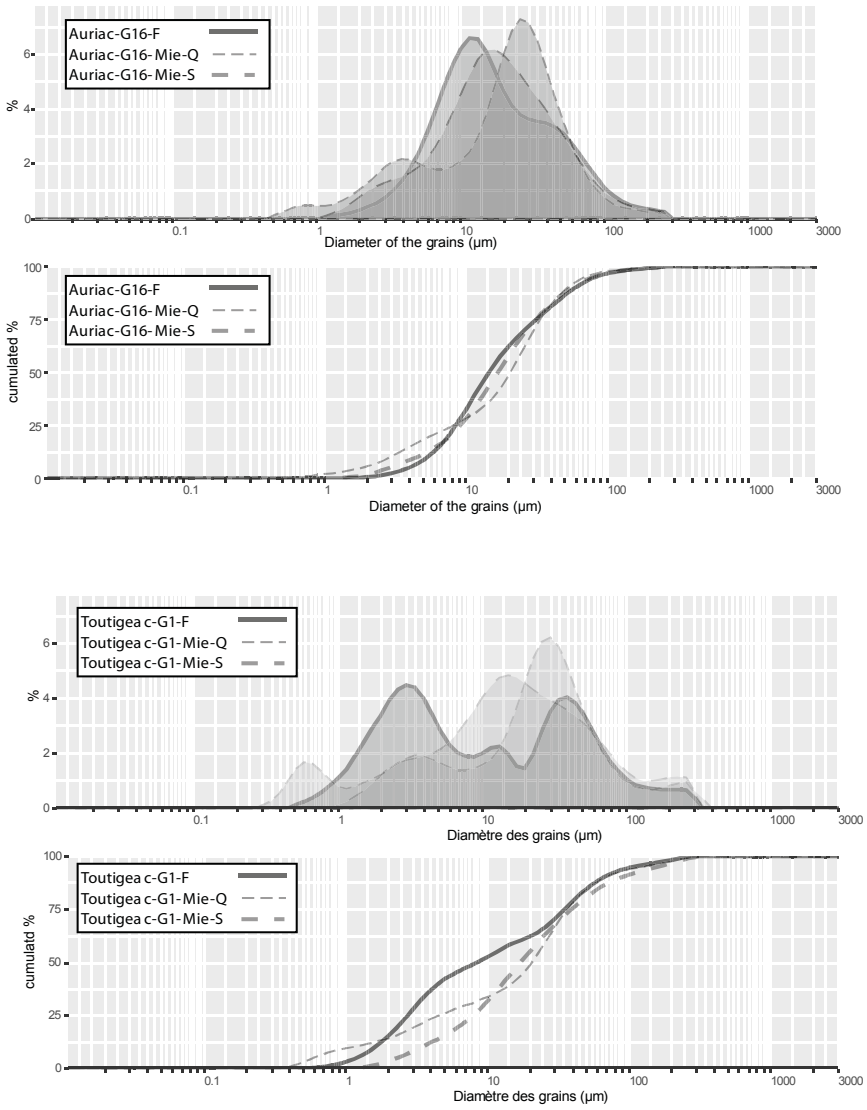

Figure SI_3: Comparison of the particle-size distribution obtained from the calculations.

2. Selection criteria for the DONESOL database

The DONESOL database is based on a relational model (Infosol 2011). The basic unit is made up of tables containing columns of data that document a specific subject (e.g. soil horizon). We selected the tables “Profile”, “Horizon” and “Analyses”, which contain all the information needed for this study. Each profile is associated with several horizons and each horizon with several analyses. The profile is the highest hierarchical level of the data set used in this study.

The data set was cleaned in order to select the profiles, horizons and analyses corresponding to aeolian deposits. Indeed, the profiles listed in the data set are distributed on several types of geological formations and in various topographical settings. A soil profile is complex when it develops on geological units of different nature and/or origin. Finally, a soil horizon does not always correspond to a single lithostratigraphic unit and may include two or more of them. Samples taken for analysis within a horizon may therefore correspond to one or more depositional units.

The requirements for selecting the data have been summarized in Figure SI_4. For each hierarchical level there are different requirements and we proceed from the highest (Table

"Profile") to the lowest hierarchical level (Table "Analysis"). The approach is illustrated by an example in Figure SI_4.

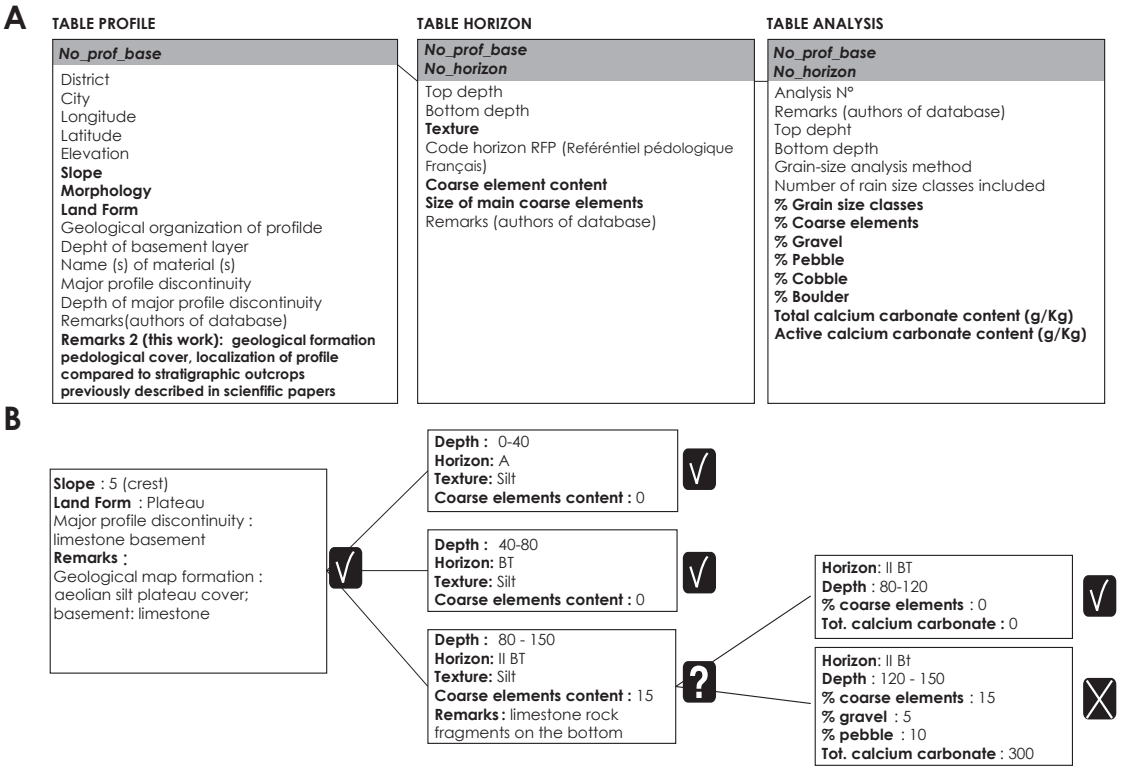

Figure SI_4: Selection of profiles among the DONESOL database. A - Conceptual scheme of the database used in this study. Dark gray: relational fields linking the different hierarchical levels. Bold: key criteria used for the selection of aeolian outcrops; B - Example of decision tree when selecting an outcrop in the database. Each step corresponds to a lower hierarchical level.

The selection of the profiles has been made using information from the 1:50,000 geological maps and, when possible (Gironde and Lot-et-Garonne districts), from soil maps. However, aeolian deposits are often not mentioned in the maps because of their low thickness or misinterpretation. Therefore, information on the distribution of aeolian deposits provided by other sources (Thibault, 1970; Dubreuilh 1976; Legigan, 1979; Ortega et al . 2005; Brenet et al., 2006; Sergent et al., 2007; Brenet et al., 2009; Fourloubey et al, 2009) were also taken into account. Only the profiles located on plateaus (very low or null slope gradient) were retained, since most profiles located on hillslopes have been potentially affected by colluviation and some mixing of the aeolian sediment with the underlying substrate may have occurred.

Within the "Horizon" table, the selection was based primarily on the texture and the abundance of coarse (> 2 mm) elements, set to zero. This allowed to exclude colluvium but also, in many cases, the ploughed horizons. Some exceptions were made for (1) aeolian sands that can have sometimes a significant coarse component (small gravel, ventifacts); (2) B horizons of luvisols rich in ferro-manganic concretions. The presence of concretions is often reported in the database.

For the "Analysis" table, three criteria were considered: (1) the grain-size composition of the fine (< 2 mm) fraction; (2) the percentage of the coarse (> 2mm) fraction; and (3) the total calcium content. The first criterion was especially useful to distinguish aeolian silts from the underlying fluvial, usually sandy formations (Miocene clayey sands, Quaternary terraces). The

second criterion was used to remove the samples containing coarse particles, which may reflect sediment mixing resulting from colluviation. The third criterion was based on the finding that the aeolian deposits of Aquitaine are not calcareaous (Bertran et al, 2011; Legigan 1979). For this reason, the total calcium content was used for discriminating loess material from other silty deposits, particularly Mesozoic marls which outcrop extensively in the basin.

3. Data preprocessing

Prior to the geostatistical analysis, the samples collected in cross-sections and those selected from the DONESOL database were treated as follows:

(a) The clay component was excluded from the calculation because this fraction may migrate during soil formation, both vertically (illuviation) and laterally, or may be affected by weathering and solubilisation. Thus, integration of the clay component carries the risk of observing variations (intra and inter profile) which reflect soil formation processes.

(b) Means were calculated for each profile from all available analyses, according to the principles of compositional analysis (Egozcue and Pawlowsky-Glahn, 2011). A profile is, thus, represented by a single composition.

4. Criteria for selection of the thickness of aeolian deposits

The selection of the loess outcrops reported by Thibault (1970) and the profiles from the DONESOL database was made following the same criteria used for the selection of the samples for grain size (Fig SI_4). Nevertheless, the slope was not a discriminating criterion for choosing a profile or an outcrop to document the loess thickness. Indeed, our interest in this case was to describe the spatial variability of the thickness of the aeolian mantle and, as a consequence, the sites on slope were just as interesting as those located on the plateau. This implied that the profiles or outcrops potentially corresponding to colluvium of aeolian sediment on slopes were included in the data set.

5. Geostatistics : variographic analysis of grain-size data

As already specified in the paper, we carried out a variographic analysis (Webster and Oliver, 2007) in order to obtain a robust spatial interpolation of grain-size composition and loess thickness. For grain-size data, in agreement with Pawlowsky and Burger (1992), each variable was transformed before variographic analysis using the Isometric Logratio Transformation (IRL) (Egozcue et al., 2003). Applied to our case, the *IRL* transforms our four-part composition (% coarse sand, % fine sand, % coarse silt, % fine silt) into three "coordinates", or compositional variables (b1, b2, b3 – see Fig. SI.5 for the formulas corresponding to this variables). This transformation allows a correct treatment of the compositional data during the process of variographic analysis. Here we detail the main steps we followed in order to clarify our geostatistical approach and choices. Then, as suggested by Pawlowsky and Burger (1992), we applied the inverse transform to our compositional variables b1, b2 and b3 in order to realize the final maps showing the sand and silt content of the loess deposits.

Compositional variables

Figure SI_5 shows the frequency histograms of the compositional variables (b1, b2, b3) obtained after isometric log-ratio transformation of grain-size data (coarse sand, fine sand, coarse silt,

fine silt). The results of the Anderson-Darling test always reject the hypothesis of normality of the distribution (Fig. SI_5). The adjustment to a normal distribution of a variable is not fundamental because the calculation of the variogram and the estimation of values are not affected by normality (Gutjahr, 1984 in Chery, 1995). When a variable has a normal distribution, it is possible to calculate confidence intervals based on the standard deviation of estimated values obtained by kriging.

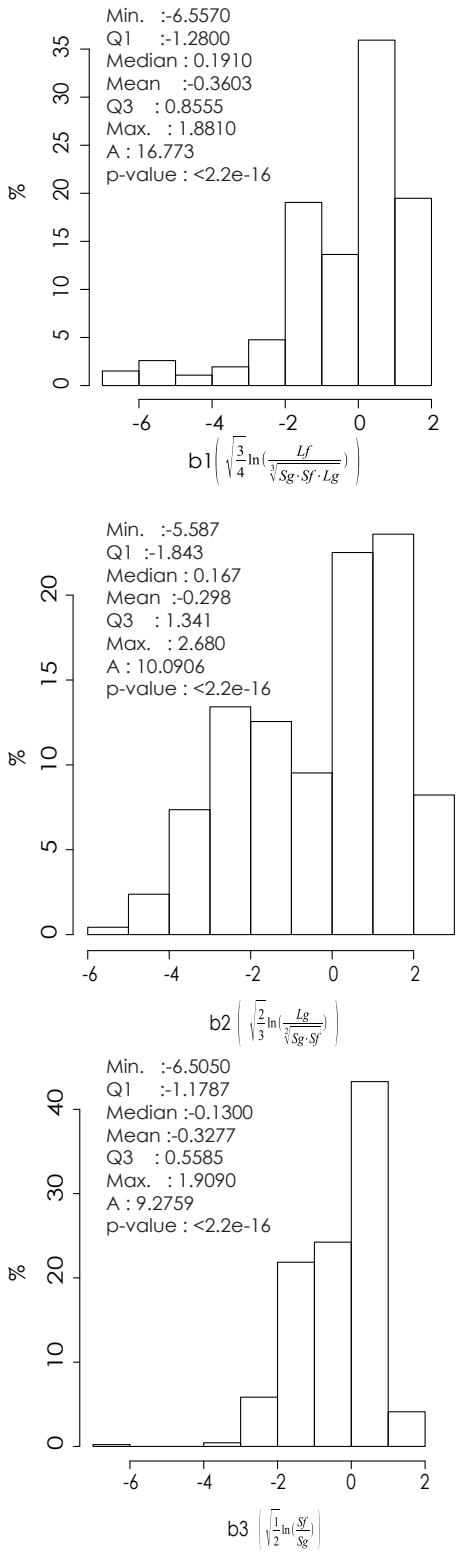

Fig. SI_5: Frequency histograms of three log-variables b1, b2, b3, obtained by isometric log-ratio transformation of the four original grain-size variables (% coarse sand (Sg),% fine sand (Sf)% coarse silt (Lg) %, fine silt (Lf)). The value A is the result of the Anderson-Darling test where a p-value> 0.05 indicates a normal distribution.

Variograms

Experimental variograms were built using the following protocol: for each variable, and both for omnidirectional and directional variograms, we used the same lag distance (h) and search the neighbourhood distance. The parameters used are summarized in table SI_2. The number of pairs of points according to the distance h is presented in Table SI_2. This number is always greater than the threshold of 50 pairs and allows us to consider the variograms as reliable.

A

Min & Max X (m)	Min & Max Y (m)	Number of lags	Neighborhood search distance (m)
300680 - 432282	1843700 - 2040502	10	10000

B

		Number of pairs				
Lag	Class of distance	Omnidirectionnal	0 (E-0)	45 (NE-SW)	90 (N-S)	135 (NW-SE)
0	0-3000	6298	1808	1443	1343	1711
1	3000-10000	12360	3719	2314	2461	3868
2	10000-20000	12106	4083	3361	1970	2692
3	20000-30000	13584	5127	3815	1665	2977
4	30000-40000	13524	4585	3196	2177	3566
5	40000-50000	15984	3768	3969	4224	4023
6	50000-60000	13634	2182	2971	4635	3846
7	60000-70000	11128	1811	2948	3753	2616
8	70000-80000	9634	1445	2355	3372	2462
9	80000-90000	11302	1494	2819	4157	2832
10	90000-100000	10332	796	3211	4370	1955

Table SI_2: Parameters used for the construction of the experimental variograms in the case of grain-size data.

The variograms are shown in Figure SI_6. The nugget effect, which is related to spatial variations smallest than the minimal sampling intervalo or to errors of measurement (Webster & Oliver, 2007), is very small for the variables b2 and b3, while it is more important for the b1 variable. For each variable, there is no actual difference between the experimental and the directional variograms. This reveals a lack of spatial anisotropy. Thus, for each variable, the theoretical model was established based on the omnidirectional variogram. The goodness of fit of the experimental to the theoretical variograms have been obtained for all variables, using Gaussian and spherical models. In our case, these two models always slightly differ, the Gaussian model being apparently more efficient for the variables b1 and b2. Despite this, we preferred applying the spherical model every time. Indeed, the Gaussian model passes close to the x axis with a gradient near zero and this property may involve instabilities in kriging equations and estimates (Wackernagel, 2003; Webster and Oliver, 2007). The theoretical variogram for b1, b2 and b3 is shown in Figure SI_7, while the parameters of the variograms and the goodness of fit values are summarized in Table SI_3.

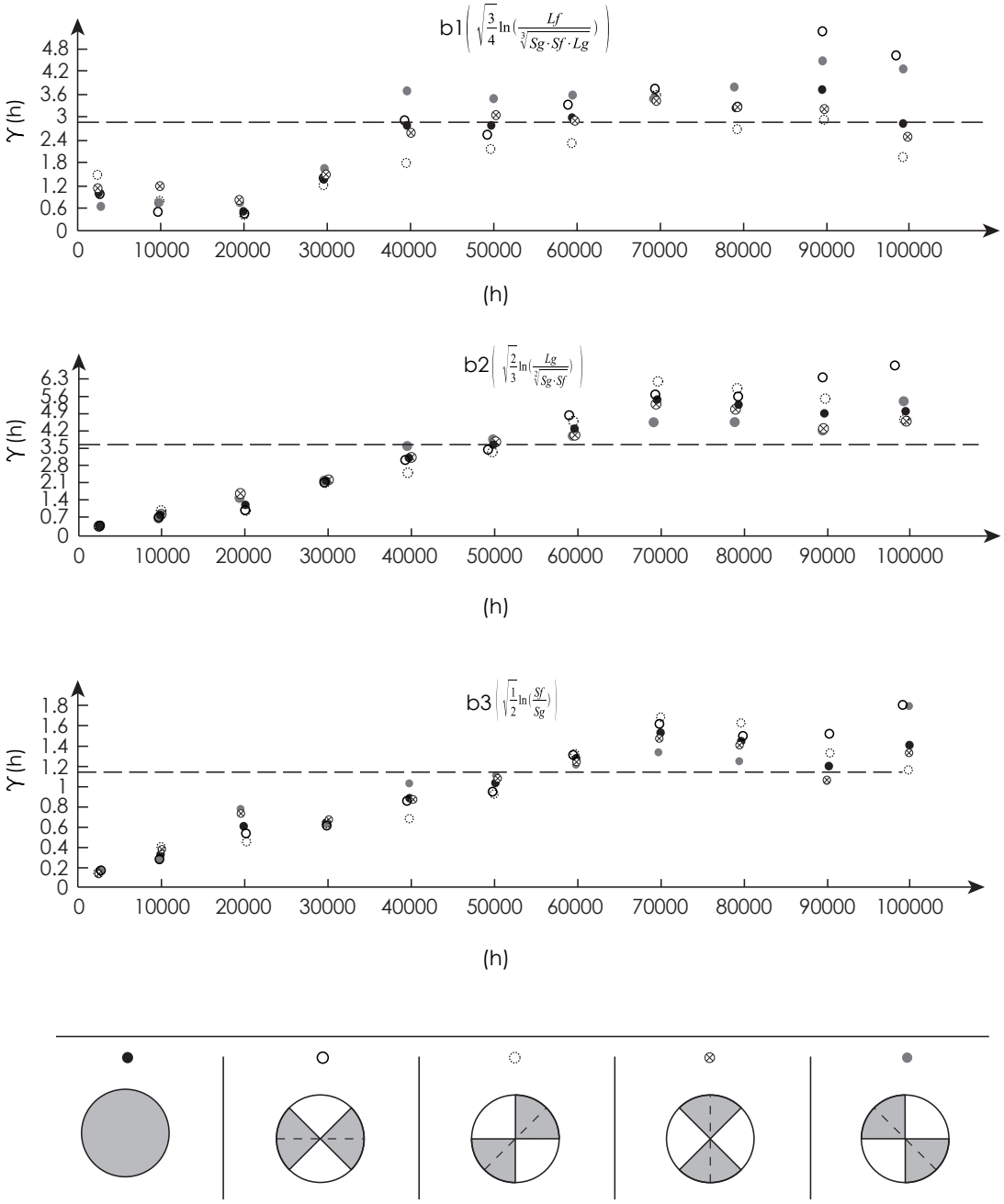

Figure SI_6: Experimental variograms of the three log-variables b1, b2, b3, obtained by isometric log-ratio transformation of the four original particle size variables (% coarse sand (Sg), % fine sand (Sf), % coarse silt (Lg), % fine silt (Lf)). Directional variograms were done at 45° intervals proceeding counterclockwise. Here, the 0 corresponds to the direction E-W. The direction corresponding to each symbol is indicated at the bottom of Fig. H = distance between pairs of points; γ (h) = semi-variance.

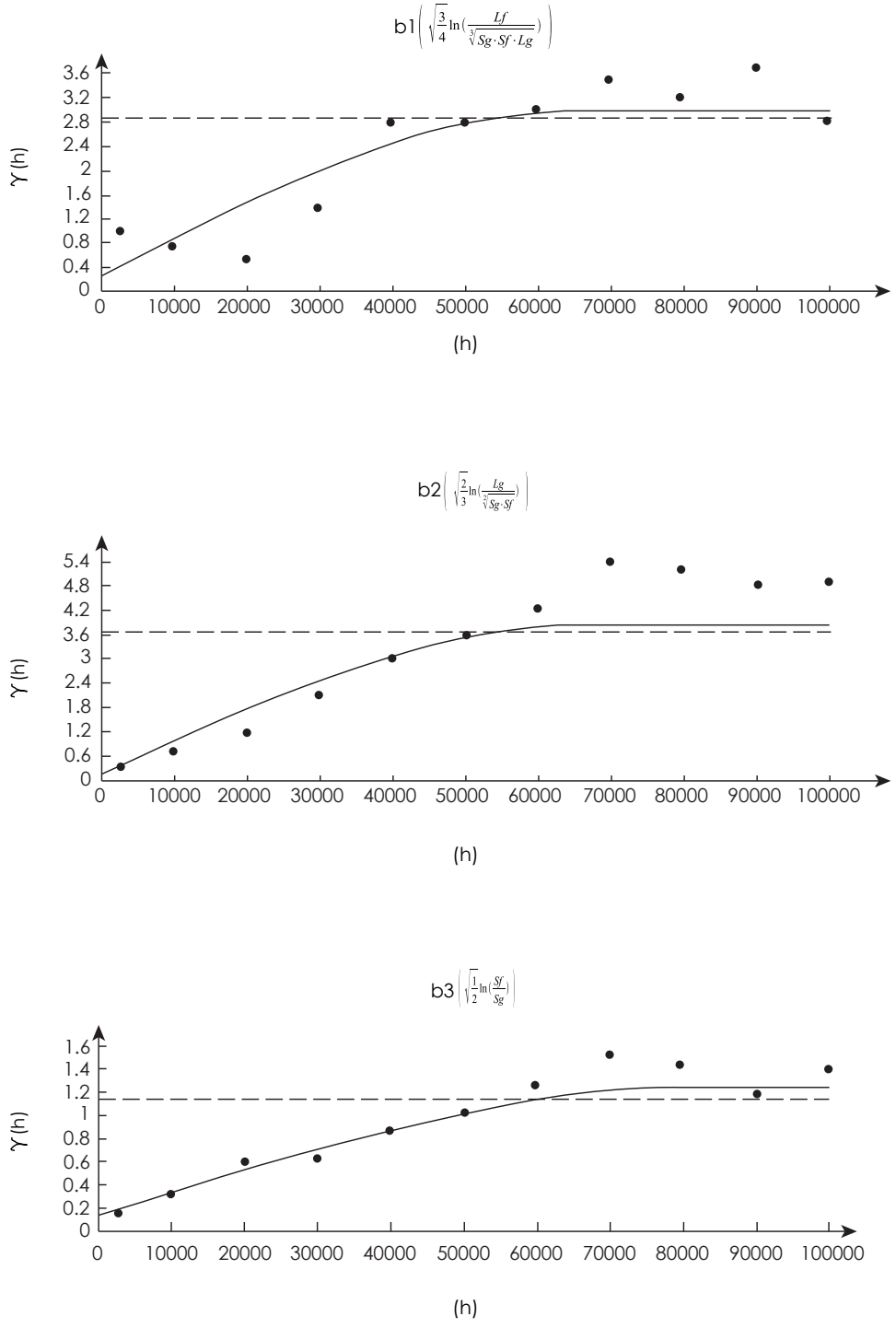

Figure SI_7: Theoretical variograms of the three log-variables b1, b2, b3, obtained by log-ratio isometric transformation of the four original particle size variables (% coarse sand (Sg), % fine sand (Sf), % coarse silt (Lg), % fine silt (Lf)). H = distance between pairs of points; γ (h) = semi-variance.

b1

Model	c_0	c	a	IGF
Spherical	0.29	2.692	64996	0.153
Exponential	0.464	2.9	93496	0.261
Gaussian	0.667	2.9	74796	0.135

b2

Model	c_0	c	a	IGF
Spherical	0.148	3.7	66000	0.074
Exponential	0.074	3.7	51696	0.27
Gaussian	0.407	3.7	59396	0.06

b3

Model	c_0	c	a	IGF
Spherical	0.144	1.116	83200	0.021
Exponential	0.108	1.128	87100	0.057
Gaussian	0.18	1.2	66300	0.025

Table SI_3: Parameters of theoretical variograms in the case of particle size data and Goodness of fit value (IGF) for each variable used. C0 = E and nugget; C = sill a = range; IGF = Goodness of Fit.

Kriging and cross-validation

The kriging of the three variables was carried out using a minimum number of seven neighbours and a subdivision in four sectors lasting 45° from each other for the estimation. The results of cross-validation are presented in Table SI_4. The mean error is close to zero and the mean square deviation ratio is close to one for the three variables. As expected, the variable b1 had the most significant errors since the theoretical variogram had the worst values of adjustment. Nevertheless, we obtained acceptable values and kriging can be considered satisfactory.

Variable	Model	ME	MSDR
b1	Spheric	-0,006895	1,24
b2	Spheric	0,02834	1,092
b3	Spheric	0,005999	1,106

Table SI_4: Results of cross-validation for ordinary kriging of particle size data according to each one of the three log-variables. ME = mean error; MSDR = mean square deviation ratio.

For cross-validation through the independent data set (N = 51), we first tested if there was a significant difference between ordinary kriging of untransformed compositional data and ordinary kriging of transformed compositional data. The value of standardized residual sum of squares (STRESS) was equal to 0.55 for transformed data and 0.74 for unprocessed data. So, we can already conclude that the transformation of grain-size data we performed following Pawlowsky-Glahn and Olea (2004) significantly reduces the estimation errors in our data set. However, it has to be noticed that the value of 0.55 is fairly high since it means that, overall, the agreement between estimated and real data is bad for 55% of cases.

The frequency histogram of distance values between estimated and real data shows that 86% are distance values lower 2, while 13% are more extreme (Fig. SI_8). These extremes are probably at the origin of such a high value of STRESS. For example, we try to remove the three

samples at the origin of the highest values of distance. We consequently obtained a STRESS value of 0.48. On the other hand, the independent data set is constituted by a relatively small number of samples compared to the data set used for the kriging. It is, therefore, quite sensitive to extreme data.

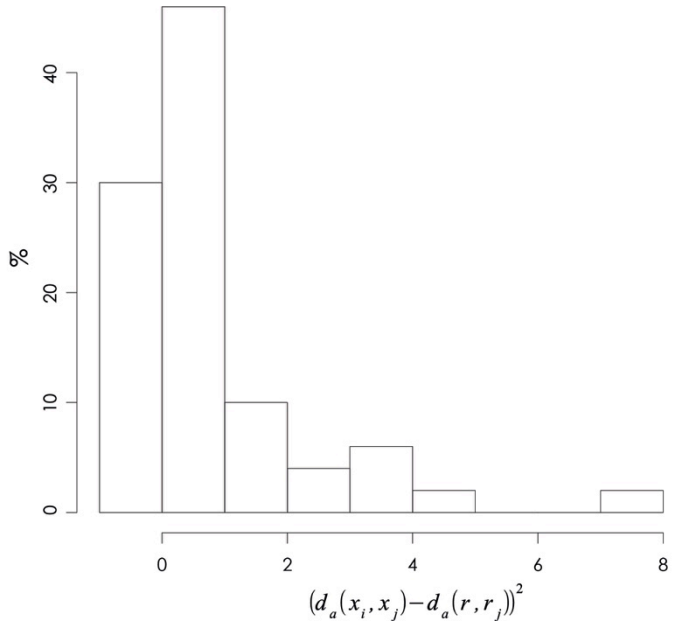

Figure SI_8: Frequency histogram of the estimated distance between estimated values (modeled by ordinary kriging content in coarse sand, fine sand, coarse and fine silt) and real values (independent data set). The distance is the Aitchison distance (Pawlowsky-Glahn and Buccianti, 2011).

6. Geostatistics: variographic analysis of aeolian silt thickness

The frequency histograms of loess thickness for the northern and southern data sets are shown in Fig SI_9. In the North, the distribution of values is always positively asymmetrical, the class of values around zero dominating; in the South, the distribution of values is more heterogeneous. The results of the Anderson-Darling test for data sets reject the hypothesis of adjustment to a normal distribution. However as we said earlier, the normality of the values is not a mandatory prerequisite for the kriging.

Experimental variograms were constructed following the protocol used for particle size data. The main parameters are presented in Tables SI_5 and 6. For all selections, the number of pairs is above the threshold of 50, apart for one directional variograms (dir = 90) of the southern data set. Overall, the number of couples according to the direction is quite similar regarding the northern data set. A greater variability is observed for the southern data set.

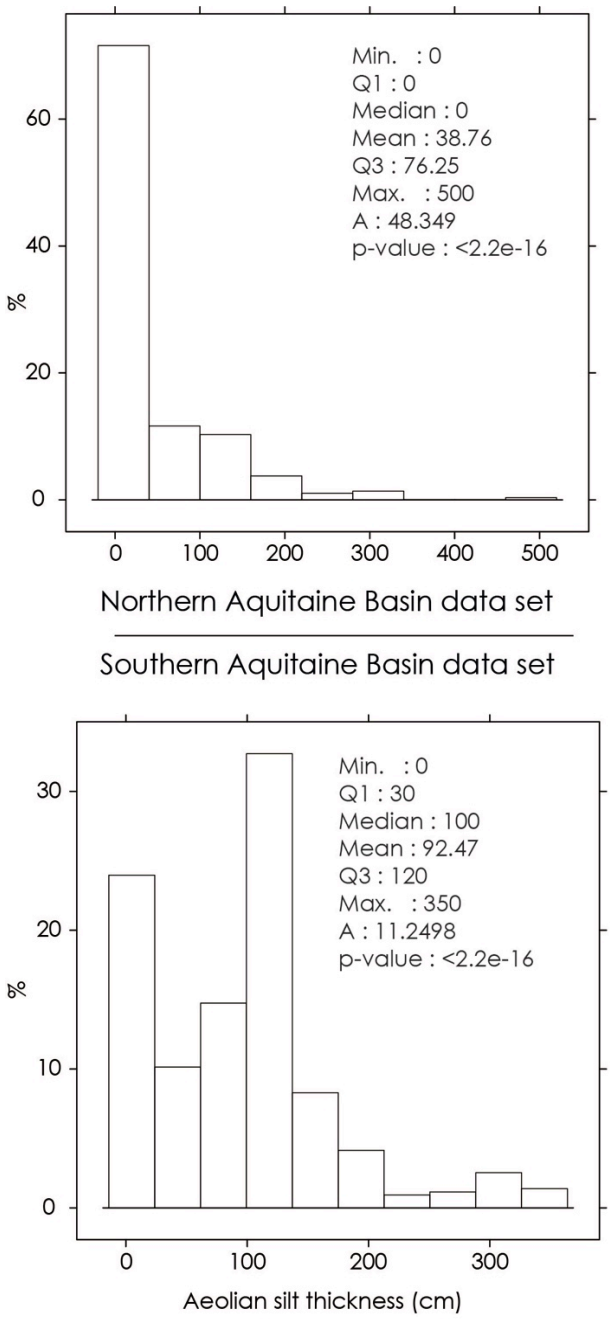

Figure SI_9: Histograms of frequency of loess thickness for the northern and southern data sets. The value A is the result of the Anderson-Darling test where a p-value> 0.05 indicates a normal distribution.

	Min & Max X (m)	Min & Max Y (m)	Number of lags	Neighborhood search distance (m)
A	364142-426748	1956097-2036380	12	2828

A

Lag	Class of distance	Number of pairs Omnidirectionnal	0 (E-0)	45 (NE-SW)	90 (N-S)	135 (NW-SE)
0	0-760	690	199	482	147	164
1	760-2821	2456	590	567	638	661
2	2821-5642	3110	781	779	774	776
3	5642-8463	3406	872	842	831	861
4	8463-11284	4002	1224	1071	777	927
5	11284-14105	3964	1142	991	840	991
6	14105-16926	3216	813	825	795	783
7	16926-19747	3490	845	814	900	931
8	22568-25389	4468	922	999	1312	1235
9	25389-28210	5060	963	952	1567	1578
10	28210-31031	5884	1039	1042	1903	1908
11	31031-33852	5504	749	1063	2003	1689
12	33852-36673	5350	760	1072	1915	1603

Table SI_5: Top - parameters used for the construction of experimental variograms in the case of the northern dataset. Bottom - number of pairs by distance h in the omnidirectional case and in the case of different directions.

	Min & Max X (m)	Min & Max Y (m)	Number of lags	Neighborhood search distance (m)
A	292309 - 393100	1837959-1878132	20	2712

A

Lag	Class of distance	Number of pairs Omnidirectionnal	0 (E-0)	45 (NE-SW)	90 (N-S)	135 (NW-SE)
0	0-815	2132	548	513	525	569
1	815-2712	8096	2480	1665	1569	2384
2	2712-5424	8314	2782	1651	1375	2506
3	5424-8136	11760	3392	2805	2490	3079
4	8136-10848	14892	4033	3316	3413	4130
5	13560-16272	13664	4113	3147	2719	3683
6	16272-18984	13298	4656	3645	1993	5004
7	18984-21696	13712	5220	4065	1636	2791
8	21696-24408	13164	5382	4127	1200	2455
9	24408-27120	11272	5156	3911	480	1725
10	27120-29832	11244	5210	3963	412	1659
11	29832-32544	10872	4896	3752	540	1684
12	32544-35256	8842	4208	2814	213	1607
13	35256-37968	6986	3384	2241	109	1252
14	37968-40680	6012	2986	1926	20	1080
15	40680-43392	5074	2521	1732	16	805
16	43392-46104	4176	2087	1596		492
17	46104-48816	2998	1950	1642		312
18	48816-51528	3668	1834	1408		426
19	51528-54240	3146	1573	1262		311
20	54240-56952	2425	1213	1096		117

Table SI_6: Top - parameters used for the construction of experimental variograms in the case of the southern dataset. Bottom - number of pairs by distance h in the omnidirectional case and in the case of different directions.

The experimental variograms are characterized by (Fig. SI_10):

i. a significant nugget effect in both data sets;

ii. high variability of semi-variance values since 20 km of distance for the northern data set and about 30 km for the southern data set. Our interpretation is that this variability has to be related with the spatial distribution of the sites;

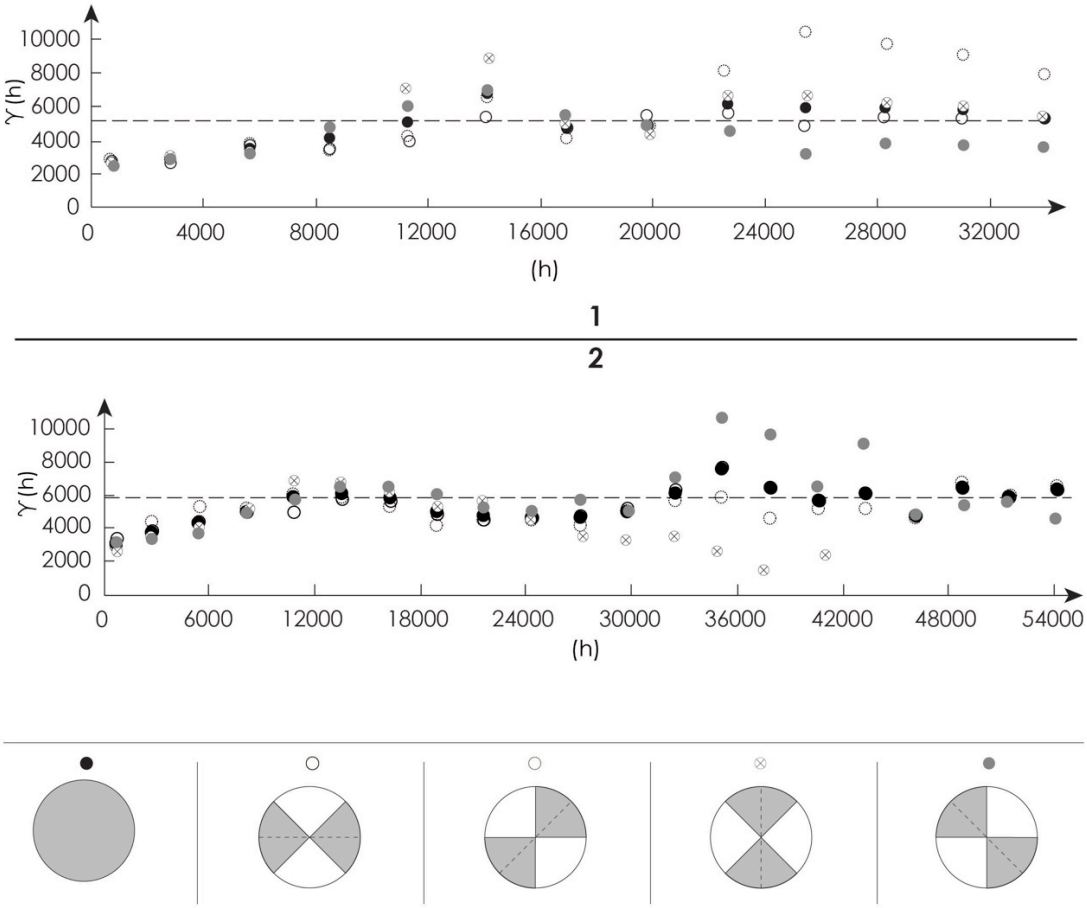

Figure SI_10: Experimental variograms for the northern (1) and the southern data sets (2) For each variable we included omnidirectional and directional variograms. Directional variograms were done at 45° intervals proceeding counterclockwise. Here, the 0 corresponds to the direction E-W. The direction corresponding to each symbol is indicated at the bottom of the Fig. H = distance between pairs of points; γ (h) = semi-variance.

The theoretical variograms have been built using a directional model for the northern data set and an omnidirectional model for the southern one. The parameters of theoretical variograms and the best goodness of fit of models are reported in Table SI_7 and the fitting functions are presented in Fig. SI_11.

For the northern Aquitaine data set, the Gaussian model provides the best fit. However, we have not considered this model due to the previously outlined problems. The theoretical variogram were instead modelled by a spherical function, considering that the fitting quality between spherical and Gaussian function is reasonably comparable. The nugget effect is about 41% of the total variance.

For the southern Aquitaine data set, the spherical model has the best goodness of fit and thus we used it to model the theoretical variogram. The nugget effect is about 46 % of the total variance.

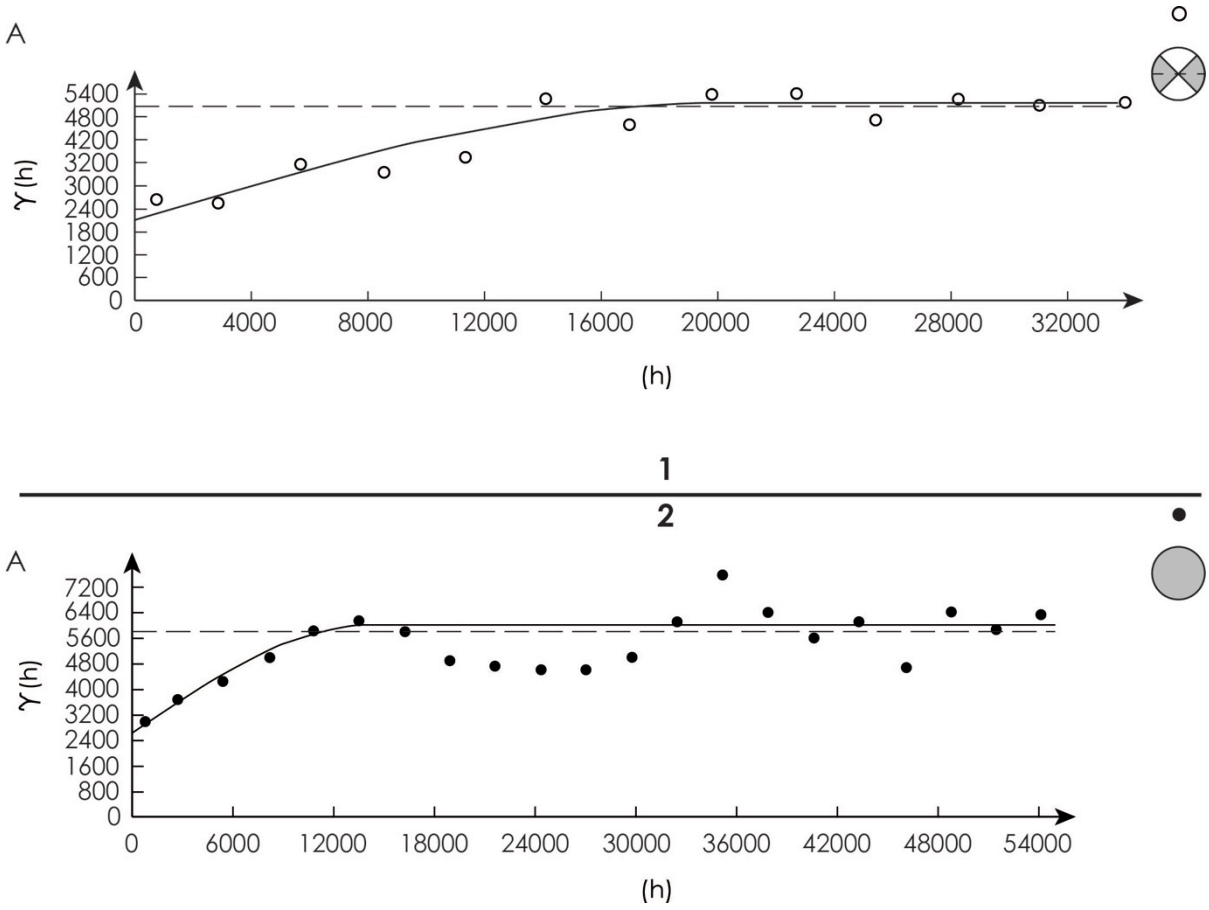

Figure SI_11: Theoretical variograms for the northern (1) and southern (2) data sets. For symbols see Fig. SI_8. H = distance between pairs of points; γ (h) = semi-variance.

Model	C_0	c	a	IGF
Spherical	**2132**	**3067.83**	**20398**	**0.021**
Exponential	1819,83	3431	24478	0.028
Gaussian	2495.83	2911.83	21078.9	0.015

Northern Aquitaine Basin data set

Southern Aquitaine Basin data set

Model	C_0	c	a	IGF
Spherical	**2668**	**3364**	**14294.5**	**0.047**
Exponential	2378	3654	15946	0.049
Gaussian	3074	3132	13194.5	0.059

Table SI_7: Parameters of theoretical variograms in the case of grain-size data and Goodness of fit value (IGF) for each variable used. C0 = E and nugget; C = sill a = range; IGF = Goodness of Fit.

Kriging and cross-validation

The ordinary kriging of loess thickness was made using the same criteria applied for the kriging of grain-size data. The results of the cross validation are presented in Table SI_8. The mean error value is close to zero, the error being stronger for the southern selection. The mean square deviation ratio is close to 1 for both data sets.

Northern Aquitaine Basin data set

Model	ME	MSDR
Spherical	0,09471	1,093

Southern Aquitaine Basin data set

Model	ME	MSDR
Spherical	0,7872	0,9812

Table SI_8: Results of cross-validation for ordinary kriging of particle size data according to each one of the data sets. ME = mean error; MSDR = mean square deviation ratio.

As for grain-size data, we realized cross-validation with an independent data set. Summary statistics for the cross-validation of northern and southern data sets is provided in Table SI_9. These results show that:

i. the means of observed and estimated data are significantly different: high for the northern data set (60.69 cm observed data *vs* 37.66 estimated data), while the difference is smaller for the southern data set (85.38 cm observed data *vs* 81.02 cm estimated data) ;

ii. the kriging interpolation systematically reduces the standard deviation of thickness values around the mean;

iii. the differences between observed and estimated values are higher for northern data set that for southern one.

The linear regression established for each data set is shown in Fig. SI_12. The most important errors are related to extreme values. This is particularly evident for estimated values which are associated with observed values equal to 0. The regression coefficient is apparently higher for the northern data set (Fig. SI_12). We have not been able to estimate the re-estimation precision and the average error for selections from the north of the basin.

The Anderson-Darling test was performed on the difference between estimated and observed values. The test results show that for southern data set the distribution of values follows a normal distribution with a probability level $\alpha = 5\%$ ($A2 > 0.787$). This allows us to estimate the accuracy of the re-estimation of the thickness values at 57.43 cm. Finally, the square root of the mean square deviation allows us to estimate an average error of 81.81 cm.

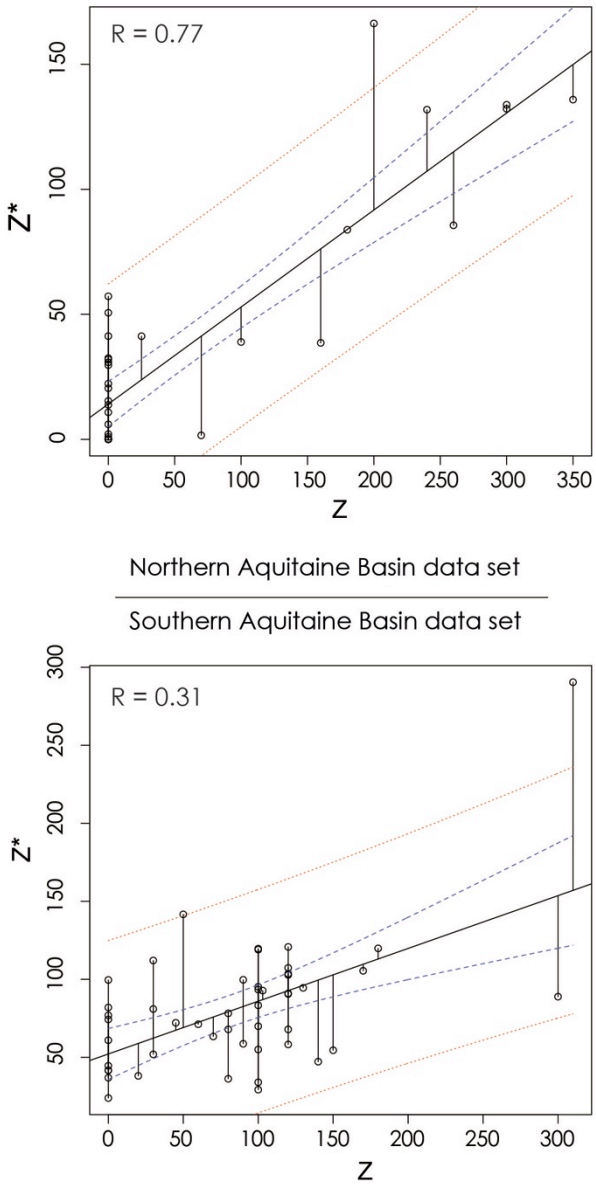

Figure SI_10: Regression of loess thickness (northern and southern data sets) between observed (z, corresponding to independent data set) and ordinary kriging estimated values (z *).

	X	Y	Z*-Z	$(Z^*-Z)^2$
Min	0	0	-214.12	0
Q25 %	0	0.15	-40.53	0.03
Median	0	21.34	0.01	456.22
Mean	60.69	37.66	-23.04	5291.09
Q75 %	77.5	43.62	17.29	3386.57
Maximum	350	166.32	57.2	45847.37
SD	91.32	73.63	69.98	10792.02
A-D Test			A = 3.5874, p-value < 2.2e-16	

Northern Aquitaine Basin data set

Southern Aquitaine Basin data set

	X	Y	Z*-Z	$(Z^*-Z)^2$
Min	0	23.9	-211.12	0.58
Q25 %	30	54.89	-32.35	291.60
Median	100	77.54	-6.6	1118.86
Mean	85.38	81.02	-4.36	3248.21
Q75 %	120	99.6	29.56	3900.83
Maximum	310	290.45	99.58	44571.65
SD	69.02	41.93	57.43	6692.89
A-D Test			A = 0.3667, p-value = 0.51	

Table SI_9: Descriptive statistics for independent datasets used in the cross validation of ordinary kriging of thicknesses in the case of northern and southern data sets. X: observed data ; Y: predicted data. Z*: predicted data; Z: observed data. A = test Anderson-Darling.

References

Bertran, P., Bateman, M.D., Hernandez, M., Mercier, N., Millet, D., Sitzia, L., Tastet, J.-P., 2011. Inland aeolian deposits of south-west France: facies, stratigraphy and chronology. Journal of Quaternary Science 26, 374–388.

Brenet M., Folgado M., Sellami F., Lenoble A., Garaizar J.R., Viellevigne E., Guibert P., 2006. Cantalouette 1 (Creysse - Dordogne). Rapport Final d'Opération, Inrap, Pessac.

Brenet M., Folgado M., Bertran P., Claud E., Vigier S., Lahaye C., 2009. Etude inter-disciplinaire des niveaux paléolithiques de Combe Brune 2 : Creysse, la déviation nord de Bergerac. Rapport Final d'Opération, Inrap, Pessac.

Bullimer, M., 2013. Automated Refractive Index Calculations for Particle Size Analysis Using Laser Diffraction. http://www.americanlaboratory.com/913-Technical-Articles/138218-Automated-Refractive-Index-Calculations-for-Particle-Size-Analysis-Using-Laser-Diffraction/ (accessed 7.20.16).

Chery P., 1995. Variabilité de l'epaisseur de la couverture de sol. Consequences pour le bilan hydrique hivernal d'un secteur de Petite Beauce. Thèse de Doctorat, Universite Henri Poincaré - Nancy 1, Nancy. 286 pp.

de Boer, G.B.J., de Weerd, C., Thoenes, D., Goossens, H.W.J., 1987. Laser Diffraction Spectrometry: Fraunhofer Diffraction Versus Mie Scattering. Particle and Particle Systems Characterization 4, 14–19.

Dubreuilh, J., 1976. Contribution à l'étude sédimentologique du système fluviatile Dordogne-Garonne dans la région bordelaise. Thèse d'état, Université de Bordeaux, Bordeaux, 273 pp.

Egozcue, J., Pawlowsky-Glahn, V., Mateu-Figueras, G., Barceló-Vidal, C., 2003. Isometric Logratio Transformations for Compositional Data Analysis. Mathematical Geology 35, 279–300.

Egozcue, J.J., Pawlowsky-Glahn, V., 2011. Basic Concepts and Procedures, in : Pawlowsky-Glahn, V., Buccianti, A. (Eds.), Compositional Data Analysis. John Wiley & Sons, Ltd, pp. 12–28.

Fourloubey C., Claud E., Lenoble A., Pasty S., Vigier S., 2009. Bourrut, Quartier Saint-Jacques (Montaut, Landes). Rapport Final d'Opération, Inrap, Pessac.

Hergert, W., Wriedt, T., 2012. The Mie Theory: Basics and Applications, Springer Series in Optical Sciences. Springer Berlin Heidelberg. 259 pp.

ISO, 2009. ISO 13320, Particle size analysis -Laser diffraction methods.

INFOSOL, 2011. Donesol version 2.0.5. http://acklins.orleans.inra.fr/outil/donesol/dictionnaire_donesol_igcs_2011-02-25.pdf (accessed 05.07.2016).

Jones, R.M., 2003. Particle size analysis by laser diffraction: ISO 13320, standard operating procedures, and Mie theory. American Laboratory.

Legigan, P., 1979. L'élaboration de la formation du Sable des Landes, Mémoire de l'Institut de Géologie du Bassin d'Aquitaine, Bordeaux, 429 pp.

Ortega I., Fourloubey C., Bertran P., Grigoletto F., Beugnier V., 2005. Les Sablons (Marsas, Gironde), Rapport Final d'Opération, Inrap, Pessac.

Mie, G., 1908. Beiträge zur Optik trüber Medien speziell kolloidaler Goldlösungen. Annalen der Physik 25, 377–445.

Pawlowsky, V., Burger, H., 1992. Spatial structure analysis of regionalized compositions. Mathematical Geology 24, 675–691.

Pawlowsky-Glahn, V., Olea, R.A., 2004. Geostatistical analysis of compositional data. Oxford University Press, Oxford, 204 pp.

Pawlowsky-Glahn, V., Buccianti, A., 2011. Compositional Data Analysis: Theory and Applications. John Wiley & Sons, UK, 378 pp.

Sergent F., Lenoble A., Fouéré P., 2007. Meilhan, Bois de Marsacq, Rapport Final d'Opération, Inrap, Pessac.

Thibault, C., 1970. Recherches sur les terrains quaternaires du bassin de l'Adour. Thèse d'état, Université de Bordeaux, Bordeaux, 814 pp.

Wackernagel, H., 2003. Multivariate geostatistics : an introduction with applications. Springer, New York, 387 pp.

Webster, R., Oliver, M.A., 2007. Geostatistics for environmental scientists. Statistics in practice. Wiley, Chichester, 315 pp.